Natural variation in salt-induced changes in root:shoot ratio reveals *SR3G* as a negative regulator of root suberization and salt resilience in Arabidopsis

Maryam Rahmati Ishka[1], - ORCID - 0000-0002-5447-643X - mri23@cornell.edu
Hayley Sussman[1], - ORCID - 0000-0002-1331-3319 - hs995@cornell.edu
Yunfei Hu[2], - ORCID - 0009-0004 -9799-7798 - huyf19@lzu.edu.cn
Mashael Daghash Alqahtani[3], - ORCID - 0000-0003-0043-0847 - mdalqahtani@pnu.edu.sa
Eric Craft[4], - ORCID - 0000-0003-0966-8296 - ejc35@cornell.edu
Ronell Sicat[5], - ORCID - 0000-0001-7037-1614 - ronell.sicat@kaust.edu.sa
Minmin Wang[6], - ORCID - 0000-0001-9545-7895 - minwang@ucdavis.edu
Li'ang Yu[1], - ORCID - 0000-0002-9556-011X - ly76@cornell.edu
Rashid AitHaddou[5], rachid.aithaddou70@gmail.com
Bo Li[2] - ORCID - 0000-0002-3603-3352 - li_bo@lzu.edu.cn
Georgia Drakakaki[6], - ORCID – 0000-0002-3949-8657 - gdrakakaki@ucdavis.edu
Andrew Nelson[1], - ORCID - 0000-0001-9896-1739 - an425@cornell.edu
Miguel Pineros[4], ORCID - 0000-0002-7166-1848 - map25@cornell.edu
Arthur Korte[7], - ORCID - 0000-0003-0831-1463 - arthur.korte@uni-wuerzburg.de
Lukasz Jaremko[8], lukasz.jaremko@kaust.edu.sa
Christa Testerink[9], - ORCID - 0000-0001-6738-115X - christa.testerink@wur.nl
Mark Tester[3], - ORCID - 0000-0002-5085-8801 mark.tester@kaust.edu.sa
Magdalena M. Julkowska[1,3]* - ORCID - 0000-0002-4259-8296
*- Corresponding author mmj55@cornell.edu

Affiliations:
1 - Boyce Thompson Institute, Ithaca, NY, USA
2 - Lanzhou University, Lanzhou, China
3 - Center for Desert Agriculture, King Abdullah University of Science and Technology, Thuwal, Saudi Arabia
4 - USDA-ARS, Ithaca, NY, USA
5 - Visualization Core Lab, King Abdullah University of Science and Technology, Thuwal, Saudi Arabia
6 - UC Davis, Davis, CA, USA
7 - Julius-von-Sachs-Institute & Center for Computational and Theoretical Biology, JMU, Wuerzburg, Germany
8 - King Abdullah University of Science and Technology, Thuwal, Saudi Arabia
9 - Wageningen Research and University, Wageningen, The Netherlands

Abstract

Soil salinity is one of the major threats to agricultural productivity worldwide. Salt stress exposure alters root and shoot growth rates, thereby affecting overall plant performance. While past studies have extensively documented the effect of salt stress on root elongation and shoot development separately, here we take an innovative approach by examining the coordination of root and shoot growth under salt stress conditions. Utilizing a newly developed tool for quantifying the root:shoot ratio in agar-grown Arabidopsis seedlings, we found that salt stress results in a loss of coordination between root and shoot growth rates. We identify a specific gene cluster encoding domain-of-unknown-function 247 (DUF247), and characterize one of these genes as Salt Root:shoot Ratio Regulator Gene (SR3G). Further analysis elucidates the role of SR3G as a negative regulator of salt stress tolerance, revealing its function in regulating shoot growth, root suberization, and sodium accumulation. We further characterize that *SR3G* expression is modulated by *WRKY75* transcription factor, known as a positive regulator of salt stress tolerance. Finally, we show that the salt stress sensitivity of *wrky75* mutant is completely diminished when it is combined with *sr3g* mutation. Together, our results demonstrate that utilizing root:shoot ratio as an architectural feature leads to the discovery of new stress resilience gene. The study's innovative approach and findings not only contribute to our understanding of plant stress tolerance mechanisms but also open new avenues for genetic and agronomic strategies to enhance crop environmental resilience.

Introduction

Salt stress is predominant in the dryland areas where evaporation rate exceeds water input, resulting in increased accumulation of salts in the upper soil layers (Abrol, Yadav, and Massoud 1988; Fischer et al. 2021; Richards 1969). Dryland areas of South America, southern and western Australia, Mexico, southwest United States, and South Africa were previously identified as primary hotspots for soil salinization (Hassani, Azapagic, and Shokri 2021). As fresh water becomes scarcer, understanding the mechanisms of salt stress resilience becomes of paramount importance in the context of global agricultural productivity and sustainability.

Salt stress detrimentally affects plant growth and development, decreasing the activity of the meristem (West, Inzé, and Beemster 2004). Studies utilizing main root elongation as an indicator of salt tolerance have led to identification of many crucial components of salt stress signaling and tolerance, including genes involved in salt-overly sensitive signaling (SOS) pathway, jasmonate , ethylene, abscisic acid (ABA), reactive oxygen species (ROS) in glycophytes and halophytes alike (Wu, Ding, and Zhu 1996; Valenzuela et al. 2016; Yunfei Hu et al. 2023; Geng et al. 2013; Fu et al. 2019; Şekerci et al. 2023). Additionally, negative halotropism response, that describes a directional growth of main root away from the salt gradient, was used to identify a wide range of molecular components regulating the auxin redistribution and cell-wall remodeling, to actively avoid high salt (Galvan-Ampudia et al. 2013; Deolu-Ajayi et al. 2019; B. Yu et al. 2022; Korver et al. 2020; Y. Zou et al. 2022). The development of lateral roots is affected by salinity, and the differential effect on main and lateral roots within specific genotype can result in substantial reprogramming of root system architecture (Julkowska et al. 2014, 2017). The shoot development is impacted by salt stress, as the salt impacts the plant transpiration and photosynthetic efficiency instantaneously (Awlia et al. 2016, 2021; Julkowska et al. 2016). Many forward genetic studies were highly successful in associating natural variation in root and shoot growth with underlying genes (Awlia et al. 2021; Julkowska et al. 2016, 2017). However, these studies typically focus on either above or below ground tissue.

The coordination of root and shoot growth rate is an important aspect of seedling establishment, and becomes even more critical under abiotic stress (Karcher et al. 2008; Xu et al. 2015; Chen et al. 2022; Y. Wang et al. 2018; Bacher et al. 2022). The importance of increased root:shoot ratio, maximizing water scavenging while limiting transpiration, is well studied under drought stress (Asch et al. 2005; Karcher et al. 2008; Uga et al. 2013; Chen et al. 2022). However, the effect of salt stress on root:shoot ratio is yet to be described, and its contribution to salt stress remains unknown. Here, we developed a tool to quantify root:shoot ratio from agar-grown Arabidopsis seedlings, and re-analyzed the natural diversity panel of Arabidopsis exposed to salt stress (Julkowska et al. 2017). We have observed that while salt stress does not elicit a clear response in root:shoot ratio, it results in loss of coordination of root and shoot growth rates. The locus associated with salt-induced changes in root:shoot ratio consisted of a gene cluster encoding domain-of-unknown-function 247 (DUF247), with majority of SNPs clustering into one specific gene (At3g50160), that we named as Salt Root:shoot Ratio Regulator Gene (SR3G). Further characterization of SR3G revealed its function as a negative regulator of salt stress resilience, through regulation of root suberization, shoot growth, and Na^+ accumulation. We found WRKY75 transcription factor, a positive regulator of salt stress tolerance, acts upstream of SR3G, binding directly to the SR3G promoter in yeast. While *sr3g* and *wrky75* mutants showed contrasting salt stress response, the double mutants of *sr3g/wrky75* displayed reduced sensitivity to salt stress.

Materials & Methods

Screening HapMap population for the increase in root and shoot size

The images collected within (Julkowska et al. 2017) were re-analyzed in this manuscript to examine salt-induced changes in the root:shoot ratio for the data presented here. 360 accessions of the Arabidopsis HapMap population (Weigel and Mott 2009) were screened over 7 experimental batches, using 4 biological replicates per genotype per condition. The seeds were surface sterilized, incubated in sterile MQ water at 4°C for 48 h, and germinated on media containing ½ Murashige-Skoog, 0.5% sucrose, 0.1% MES buffer, pH 5.8 (KOH) and 1% Dashin agar. The 4-day-old seedlings were subsequently transferred to media additionally supplemented with 0, 75 or 125 mM NaCl. The plates were scanned every 2nd day using a flat-bed scanner for 8 consecutive days.

The collected images were analyzed for green and white pixels, corresponding to the projected surface of the shoot and root, respectively (https://github.com/ronellsicat/PlantSeg). A Matlab-based tool was developed and used to simplify and speed up the segmentation and analysis pipeline. For automatic segmentation, the tool uses a combination of image operations (histogram equalization), thresholding on different color spaces (e.g., RGB, YCbCr, Lab, HSV), and binary image processing (boundary and islands removal). For analysis, the tool uses connected components analysis to extract the plants (combined roots and shoots) and can guide the user to find possible mistakes which can be manually corrected via the user interface. After segmentation, the number of pixels for roots and shoots are counted and recorded automatically. More details are provided in the publicly available repository for the tool (https://github.com/ronellsicat/PlantSeg). The collected images and corresponding data acquired from them using the tool can be accessed at Zenodo Repository (experimental batch 1: https://doi.org/10.5281/zenodo.7272155; experimental batch 2: https://doi.org/10.5281/zenodo.7272344; experimental batch 3: https://doi.org/10.5281/zenodo.7272647; experimental batch 4: https://doi.org/10.5281/zenodo.7271841; experimental batch 5: https://doi.org/10.5281/zenodo.7272139; experimental batch 6: https://doi.org/10.5281/zenodo.7273936; experimental batch 7: https://doi.org/10.5281/zenodo.7273937; quantified data: https://doi.org/10.5281/zenodo.7268673). The tool's precision was evaluated by growing the Col-0 seedlings on agar plates, analyzing their root and shoot projected area on the final day using the tool, and correlating it with the recorded fresh and dry weight of the seedlings (**Fig. S1**). The collected data from the HapMap panel was analyzed using R for potential outliers (samples identified to be more than 3x standard deviation from the mean of each genotype within each condition), and the genotype-specific mean was calculated using the stats package (Team et al. 2018). The overall increase in root and shoot area was investigated for differences between control and salt stress conditions (**Fig. S2**). The root and shoot growth were estimated by fitting a linear function for a log-transformed projected root or shoot area over the non-transformed timeline of the experiment (https://rpubs.com/mjulkowska/HapMap-root-shoot-data). The data were subsequently used to explore differences between the experimental batches and the standard deviations within individual accessions. The genotypes above 3 standard deviations from the population's mean were excluded from further analysis. The salt tolerance index (STI) was calculated for root and shoot growth by dividing the average trait value at salt stress by the genotype-specific average at control conditions (**Fig. S3**). The correlations between individual traits were examined using the genotypic mean (**Fig. S4**). All quantitative data for root and shoot growth was visualized using ggplot2, corrplot and ggpubr packages (Kassambara, n.d.; Wilke 2016; Wei and Simko 2017). For all measured traits, we estimated broad sense

143 heritability (H^2) using the MVApp (Julkowska et al. 2018) (**Table S1**). The data used as an input for GWAS
144 can be found in **Table S2**.

145 Genome-Wide Association Study

146 The genotype-specific mean was used as an input to GWAS. The GWAS was conducted as described in
147 (Awlia et al. 2021), initially using 250 k SNPs (Horton et al. 2012) and subsequently using 4 M SNPs
148 (1001genomes.org). The GWAS associations were evaluated for minor allele count (MAC) and association
149 strength above the Bonferroni threshold with -log10(p-value/#SNPs), calculated for each sub-population
150 of SNPs above threshold MAC (**Table S3**, Bonf.threshold.MAC.specific). The GWAS data was processed for
151 associations with all SNPs used to generate Manhattan and QQ-plots (R notebook for processing GWAS
152 data: https://rpubs.com/mjulkowska/GWAS-root-shoot-Arabidopsis-salt-250kSNPs). Additionally, we
153 prioritized the genetic loci where multiple SNPs were associated with individual traits, or multiple traits
154 were associated with one genetic locus. Our final selection yielded 14 associations with traits measured
155 under control conditions, while 9 and 23 associations were specific to traits measured under 75 and 125
156 mM NaCl, respectively (**Table S3**). The GWAS output files can be accessed at Zenodo Repository (GWAS
157 using 250 k SNPs: https://doi.org/10.5281/zenodo.7271751; GWAS using 4 M SNPs:
158 https://doi.org/10.5281/zenodo.7271741). For the most promising loci (**Table S4**), the sequence
159 information of 147 accessions belonging to the HapMap population was downloaded from the 1001
160 genomes project website (1001genomes.org) and aligned with ClustalO as described in (Julkowska et al.
161 2016). More details on plotting the genome divergence in the loci of interest can be found at
162 https://www.protocols.io/view/plotdivergence-for-plotting-the-natural-variation-x54v98y84l3e/v1. The
163 input and output files of Plot Divergence analysis can be found in Zenodo repository
164 (https://doi.org/10.5281/zenodo.7278021).

165 Haplotype analysis

166 For the most promising candidate loci (**Table S4**), we have identified the gene open reading frames that
167 were located within the linkage-disequilibrium of the associated SNPs. The protein-coding genes were
168 subsequently used for haplotype analysis. All the SNPs located within the gene coding region were used
169 to perform a haplotype analysis. The detailed protocol used for haplotype analysis can be accessed at
170 https://www.protocols.io/view/haplotype-analysis-of-the-cds-in-arabidopsis-thali-5jyl86n8v2wp/v1. The
171 accessions were grouped into haplotype groups depending on the combination of SNPs within the
172 protein-coding region of the gene of interest. The haplotypes represented by less than 3 accessions were
173 excluded from further analysis. The phenotypes of individual haplotypes were explored for significant
174 differences using ANOVA. The results for all investigated haplotypes can be accessed at Zenodo Repository
175 (https://doi.org/10.5281/zenodo.7277703).

176 Identification of SR3G orthologs and paralogs

177 DUF247 domain-containing orthologs from *Arabidopsis thaliana* and eight other species were identified
178 by reciprocal best BLAST within CoGe ((Nelson et al. 2018)
179 https://genomevolution.org/coge/CoGeBlast.pl) using *SR3G* (At3g50160) nucleotide sequence as query
180 with an E-value cutoff of 1.00E-10). The gene ID, species, and gene names been used in this study are
181 listed in **Table S5**. Sequence homologs were further confirmed by multiple alignments of those hits within
182 each species using Geneious Prime. Sequences with missing or incomplete DUF247 domains were
183 removed, with the exception of the mis-annotated DUF427 homologs in *Camelina sativa* which contained
184 an extraneous intron that, after removal, resulted in a set of intact DUF247 open reading frame containing
185 genes.

186 **Phylogenetic and positive selection analysis of SR3G orthologs**

187 Identified orthologs were translated into amino acid, then aligned by MUSCLE. Alignments were carefully
188 validated by manual correction. Briefly, diverged insertions were trimmed, shifted frames were adjusted,
189 and conserved regions after translation were retained for phylogeny reconstruction. Phylogenetic
190 reconstruction was performed using the RAxML (Stamatakis 2014) plug-in within Geneious (Geneious
191 Prime 2022.1.1) with the GAMMA-GTR nucleotide model, rapid bootstrapping with a parsimony search,
192 and 100 bootstraps. The distribution of *SR3G* and other DUF247 orthologs, root lengths for each branch,
193 were visualized by software Geneious Prime.

194 To characterize any potential positive selection that might exist along certain branches of the
195 inferred phylogeny, including SR3G and its orthologs, we performed a branch-site model A test on
196 branches leading to SR3G, and branches leading to the clade containing SR3G and its closet orthologs
197 using PAML4.0 (Yang 2007) as performed previously (Beilstein et al. 2015; Nelson et al. 2014). Specific
198 branches are denoted as ω0, ω1, ω2, ω3, and ω-rest). In the null hypothesis (H_0): we assigned a
199 substitution rate (ω = dN/dS) along with $0 < \omega < 1$ or ω = 1 to all branches (represented by H_0: ω0 = ω1 =
200 ω2 = ω3 = ω-rest). The alternative hypotheses (HAs) here allow the differential selections been applied to
201 respective branch(es). Specifically, the five alternative hypotheses are listed here: H_1: ω -rest branches =
202 ω0 = ω3 = ω1 ≠ ω2, H_2: ω -rest branches = ω0 = ω1 = ω2 ≠ ω3, H_3: ω -rest branches = ω0 ≠ ω1 ≠ ω2 ≠ ω3,
203 H_4: ω -rest branches ≠ ω0 ≠ ω1 ≠ ω2 ≠ ω3, H_{sep}: each branch has its unique ω value. To test these
204 hypotheses, we further validate or reject alternative hypotheses by conducting a Chi-square test based
205 on likelihood scores (Ln-L score) derived from the respective branch-site model A tests (Chi-square test
206 cutoff: $P < 0.05$).

207 **Screening candidate genes identified through GWAS**

208 The genes located within the selected loci (**Table S4**) were further inspected for their contributions to root
209 development and root:shoot ratio under control and salt stress conditions. The T-DNA insertion lines
210 (**Table S4**) were genotyped using primers listed in **Table S4**, to confirm the homozygous insertion of the
211 T-DNA within the phenotype lines. All the mutant lines were used for seed propagation in the controlled
212 growth chamber with 16/8h of light/dark period, at 22°C, 60% humidity and 200 µmole m^{-1} s^{-1} under long-
213 day conditions. The seeds of plants identified as homozygous were subsequently used for the experiment
214 on agar plates, as described before for the Genome-Wide Association Study. A detailed protocol for plate
215 assays can be accessed at https://www.protocols.io/view/plate-assay-for-identification-of-salt-stress-
216 indu-eq2lyd1mwlx9/v1. The plate images were analyzed for root system architecture using Smart Root
217 (Lobet, Pagès, and Draye 2011) and the root:shoot ratio using the tool described before for Genome-Wide
218 Association Study. The analysis of the mutant lines was performed in R. The data was first curated for
219 selecting possible outliers within a genotype and subsequently used to fit growth functions for root and
220 shoot tissues using exponential functions.

221 **Screening SR3G mutants within root:shoot locus**

222 The following T-DNA lines (listed in **Table S4**) were used for SR3G (AT3G50160) as the main GWAS
223 candidate: *sr3g-4* (SAIL_690_E12, glufosinate resistant) and *sr3g-5* (SAIL_608_C06, glufosinate resistant).
224 All T-DNA insertion alleles were in the background of Col-0 accession. The position of T-DNA insertions
225 was verified using PCR (primers listed in **Table S4**). RNAi lines targeting the neighboring of the *SR3G* or a
226 combination of *SR3G* and its neighboring *DUF247* genes included CSHL#3 targeting DUF130, CSHL#4
227 targeting SR3G, CSHL#5 targeting DUF130 and DUF170, CSHL#6 targeting DUF130 and DUF140, CSHL#7
228 targeting DUF10 and DUF150, CSHL#8 targeting DUF140 and DUF190, CSHL#10 targeting DUF180,

229 CSHL#11 targeting DUF150 and DUF170, CSHL#12 targeting DUF130, DUF140, DUF170, DUF180, and
230 DUF190, CSHL#13 targeting DUF140 and DUF170, CSHL#15 targeting DUF140, DUF170, DUF180, and
231 DUF190, CSHL#16 targeting DUF130, SR3G, and DUF170, CSHL#18 targeting DUF150 and DUF190,
232 CSHL#19 targeting DUF130, DUF140, DUF150, SR3G, DUF170, DUF180, and DUF190, CSHL#20 targeting
233 DUF130 and SR3G, CSHL#21 targeting DUF130 and DUF150, and CSHL#22 targeting DUF150 and SR3G.
234 The RNAi lines were verified using RT-qPCR, with the primers listed in **Table S4**. The following T-DNA
235 insertion alleles (also listed in **Table S4**) were used to characterize the neighboring genes of the *SR3G*
236 (AT3G50160): 120.2 (SAIL_382_A09), 140.1 (SALK_044685), 140.2 (SALK_005466), 140.3 (SALK_122700),
237 150.1 (SALK_003824), 150.3 (SALK_071080), 170.1 (SALK_009186), 170.2 (SALK_112602), 170.3
238 (SALK_008710), 170.4 (SALK_145999), 170.5 (SALK_072937), 190.2 (SALK_137791), 200.1 (SALK_113759),
239 200.2 (SALK_093701), 200.3 (SALK_129634). The primers used for genotyping PCR are shown in **Table S4**.

240 **Screening WRKY75 mutant lines and generation of *wrky75/sr3g* double mutant**

241 The following T-DNA insertion alleles were used for *WRKY75* (AT5G13080): *wrky75-1* (SALK_004954,
242 kanamycin resistant) and *wrky75-3* (SALKseq_046273, kanamycin resistant). All T-DNA insertion alleles
243 were in the background of Col-0 accession. The primers used for genotyping PCR are shown in **Table S4**.
244 Two sets of double mutant combinations were generated for *wrky75-3/sr3g-5*, with *wrky75-3* serving as
245 the maternal parent in one (referred to as line d) and *sr3g-5* serving as the maternal parent in the other
246 (referred to as line e).
247

248 **Plasmid construction and plant transformation**

249

250 For plant expression, all clones were constructed using the GreenGate cloning system (Lampropoulos et
251 al. 2013). We have generated full-length SR3G constructs, as well as three fragments - fragment A (from
252 amino acid number 1 to 216), fragment B (from amino acid number 217 to 468) and fragment C (from
253 amino acid number 469 to 503). Fragments A, B, AB, and ABC (full length) were cloned into entry vector
254 pGGC (GreenGate) with mVenus as N-terminal tag. SR3G fragments were PCR amplified using high-fidelity
255 DNA polymerase, and cloned as full-length cDNA or truncated version. The entry clone was evaluated
256 using Sanger sequencing to verify the absence of mutations. Promoters used included Ubiquitin 10
257 promoter (Norris, Meyer, and Callis 1993). The list of constructs generated within this project can be found
258 in **Table S6.** The SR3G constructs generated in this paper and their corresponding vector maps can be
259 accessed in Zenodo repository
260 (https://zenodo.org/records/10788996?token=eyJhbGciOiJIUzUxMiJ9.eyJpZCI6IjI2ZjkzZGRlLTQ3M2YtND
261 BmZS04MmM5LTNhMjQ5MGFmOWY0NiIsImRhdGEiOnt9LCJyYW5kb20iOiI3OGNmY2UwM2YyMGFkNW
262 YwYjM2ZjAwOWYyM2VjNDNiNCJ9.NRWsSWHBe4srG720PncdfFjeDXQ0dATuI2BjSnca5sD1P_GAW5vhD_
263 bxOSBIH2f8txZObh5YRWH4Hkva0pzqXQ). The final constructs were validated via vector digestion, using
264 BaeGI for the constructs with fragments A, B, and AB and PvuI for the full length SR3G construct.
265 Subsequently, we transformed them into *Agrobacterium tumerfaciens* strain *GV3101*. Plant
266 transformations were conducted using the floral dip method (Clough and Bent 1998). Transgenic plants
267 were selected for BASTA resistance (10 mg/L) for three generations, to ensure the homozygous and non-
268 segregating population of seedlings for each construct.

269 **Agar-based plate experiments for mutant lines**

270 Arabidopsis seeds were sterilized for 10 min with 50% bleach and rinsed five times using milli-Q water,
271 and germinated on ½ strength Murashige and Skoog (MS) medium containing 0.5% (w/v) sucrose, 0.1%
272 (w/v) 4-morpholineethanesulfonic acid (MES), and 1% (w/v) agar, with PH adjusted to 5.8 with KOH. After
273 24 h of vernalization at 4°C in the dark, the plates were placed in the Conviron growth chamber with the

light intensity of 130–150 µmol x m^{-2} x s^{-1} in a 16 h light / 8 h dark cycle at 21°C and 60% humidity. For plate assays, 4 days after germination, the seedlings were transferred to ½ MS media supplemented with 0, 75, or 125 mM NaCl as indicated. The plates were scanned using EPSON scanner every other day, starting from 4 days after germination until the plants were 14 days old. To analyze root system architectural traits from the scanned plate images, we used SmartRoot plugin (Lobet, Pagès, and Draye 2011) in ImageJ to trace the root, and extracted root-related features in the CSV format followed by data analysis in R (https://rpubs.com/mri23/913282)

Evaluation of plant performance under salt stress in soil

The seeds were germinated in ½ MS media for one week, as described for the agar-based plate experiments. One week after germination, the seedlings were transplanted to the pot (12 x 4 cm insert) containing the Cornell Mix soil watered to 100% water holding capacity and placed in the walk-in growth chamber with the 16 h light / 8 h dark period, 22°C and 60% relative humidity throughout the growth period. When the pots dried to the weight corresponding to 50% of their water holding capacity, they were soaked for 1 h in tap water or a 200 mM NaCl solution, resulting in an effective concentration of 100 mM NaCl based on the 50% soil water holding capacity, which corresponded to a moderate level of salt stress (Awlia et al. 2016). We then allowed the pots to be drained for 2-3 h to eliminate excess moisture. The pots were placed under phenotyping rigs equipped with an automated imaging system (L. 'ang Yu et al. 2023) and the pot weight was measured daily to maintain the reference weight corresponding to 50% of the soil water holding capacity throughout the experiment.

To evaluate the growth of soil-grown plants, we used an in-house developed automated imaging system using Raspberry Pi cameras to capture the growth dynamics over the period of two weeks (L. 'ang Yu et al. 2023). The collected images were processed using PlantCV pipeline (Gehan et al. 2017), followed by the data analysis in R, as described here (https://rpubs.com/mjulkowska/sr3g_Maryam2021OctNov).

Transient expression of SR3G constructs in tobacco epidermal leaf

Agrobacterium tumefaciens strain *GV3101* containing cellular marker free GFP (*35S::GFP* with rifampicin and spectinomycin resistant), generously provided by Professor Maria Harrison Lab at Boyce Thompson Institute, or mVenus-SR3G constructs (including *UBQ10::mVenus-SR3G-full length*, *UBQ10::mVenus-SR3G-fragment A*, *UBQ10::mVenus-SR3G-fragment B*, and *UBQ10::mVenus-SR3G-fragment AB*, all with spectinomycin and tetracycline resistant) were grown in liquid YEP medium with appropriate antibiotics overnight at 28°C while shaking. The following concentrations were used for antibiotics when used for transient transformation: spectinomycin (50 ug/ml), tetracycline (10 ug/ml), and rifampicin (12.5 ug/ml). Rifampicin and kanamycin (50 ug/ml) were used for P19 plasmid (generously provided by Maria Harrison Lab at BTI) as a silencing inhibitor. The following day, OD_{600} was measured to be 0.3-0.5. The cultures were then centrifuged at 8000x g for 2 min. The Agrobacterium pellet was resuspended in an induction buffer containing 10 mM $MgCl_2$, 10 mM MES, pH 5.6, and supplemented with 200 µM acetosyringone and was incubated for 2–4 h in the dark at room temperature. Leaves of 4-weeks-old *Nicotiana benthamiana* plants were infiltrated using a syringe. After 48 hours, the fluorescence was visualized in epidermal cells of leaf discs using confocal microscopy.

Confocal microscopy images were taken using the Leica TCS SP5 Laser Scanning Confocal Microscope with the following setting: Excitation at wavelengths of 488 nm (GFP), 514 nm (mVenus), and 561 nm (chlorophyll autofluorescence) were provided using an argon or DPSS (Diode-Pumped Solid State) laser. A spectral emission range of 505–525 nm for GFP, 526–560 nm for mVenus, and 680–700 nm for chlorophyll autofluorescence was used.

317 **Elemental analysis**

318 The elemental analysis was performed using Inductively Coupled Plasma Atomic Emission Spectroscopy
319 (ICP-AES). For analysis of Na^+ and K^+ ions in roots and shoots of plate-grown seedlings, the plants were
320 grown on ½ x MS plates as described above. After two weeks of exposure to 0, 75 or 125 mM NaCl, root
321 and shoot tissues were harvested and measured for fresh weight, rinsed in milli-Q water and collected
322 into separate paper bags that were dried at 60 °C for 2-3 days. Subsequently, the dry weight was recorded.
323 Samples were digested in double distilled HNO3, followed by the addition of 60/40 nitric/perchloric acid
324 continuing incubation at 150 °C. Samples were processed for ICP-AES analysis using a Thermo iCap 7000
325 ICP-AES after diluted to 10 ml with deionized water. For soil-grown plants, the entire rosette leaves were
326 harvested at the end of week four and underwent a similar procedure as described above. Ion content
327 was calculated per dry weight for each sample, followed by data analysis in R
328 (sr3g:https://rpubs.com/mri23/913285, wrky75/sr3g double mutants:
329 https://rpubs.com/mri23/1157092 for plate-grown and sr3g:https://rpubs.com/mri23/913299 for soil-
330 grown seedlings).

331 **Electrolyte leakage analysis**

332 The electrolyte leakage measurement was done as previously described (Ying Hu et al. 2015) with slight
333 modifications. In brief, for each plant, three leaf discs were incubated in 2 ml of distilled water for 24 h at
334 the light at room temperature with gentle shaking, followed by measuring the initial electrolyte leakage
335 using a conductivity meter (Horiba LAQUAtwin EC-11 Compact Conductivity Meter, # 3999960125). The
336 samples were then subjected to 80 °C for 2 h to release the total electrolyte, and cooled at room
337 temperature for 24 h. Final electrolyte leakage was measured the following day. The electrolyte leakage
338 percentage was calculated by dividing initial conductivity by final conductivity * 100 and followed by data
339 analysis in R (https://rpubs.com/mri23/913288 and https://rpubs.com/mri23/1102053).

340 **RT-qPCR analysis**

341 Total RNA was isolated from Arabidopsis seedlings root and shoot treated with or without 75 or 125 mM
342 NaCl for one week using the RNeasy Plant Mini Kit (Qiagen). RNA samples were cleaned at least twice
343 using RNase-free DNase (Qiagen) to remove genomic DNA contamination. One microgram of total RNA
344 was used for a reverse transcriptase reaction using iScript cDNA Synthesis Kit (Catalog #170-8891; Bio-
345 Rad). RT-qPCR analysis was conducted using iQ SYBRGreen Supermix (Bio-Rad) according to
346 manufacturer's instructions in the CFX96 real-time PCR system (Bio-Rad). *AT4G04120*
347 (*transposable_element_gene*) was used as a housekeeping gene for data normalization. RT-qPCR
348 experiments were conducted using three independent experiments, each with at least three biological
349 replicates. The list of primers used is shown in **Table S4**.

350 **Suberin staining**

351 Suberin content was examined in 6-days-old Arabidopsis roots treated with or without 75 mM NaCl for
352 two days using Fluorol Yellow 088 (FY; Santa Cruz Biotechnology Incorporation) staining. Seedlings grown
353 on agar plates (as described above for mutant screens) were incubated in a freshly prepared solution of
354 FY (0.01% [w/v] in lactic acid 85% [W/W]) at 70°C for 30 min, rinsed in milli-Q water for three times with
355 5 min each, and mounted on slides with 50% glycerol before confocal microscopy examination using
356 excitation at wavelength of 488 nm and a spectral emission range of 500–550 nm. Suberin quantification
357 was performed using the ImageJ software followed by data analysis in R
358 (https://rpubs.com/mri23/935019).

Suberin monomer quantification using Gas Chromatography–Mass Spectrometry (GC-MS)

100 - 150 Arabidopsis seedlings were grown on the plates for four complete days, transferred to 75 mM salt plate for two days, and roots were harvested in distilled water to remove any remaining agar. Each plate was treated as one biological replicate, and five plates were used for each genotype/condition. Each plate of roots was collected into a microcentrifuge tube and dried in a speed vacuum concentrator (Thermo Electron, Waltham, MA), and weighed. Approximately 1 mg of dried root were collected from each plate. Suberin monomer quantification was performed according to (Delude et al. 2017; Kreszies et al. 2019) with modifications. Dried root tissue was incubated in 1% cellulase plus 1% pectinase in 10 mM citrate buffer (pH 3.0) for two weeks, with the incubation solution changed every three days. After the cellulase/pectinase solution was removed, chloroform/methanol solution (2:1 and 1:2, v/v) were mixed with the root tissue for three days respectively, to remove lipids. The remaining root tissue was mixed with 1 ml freshly prepared 5% H_2SO_4 in methanol (v/v) and 200 µl of toluene containing 20 µg of heptadecanoic acid as internal standard, sealed in an 8 ml capped tube and heated at 85°C for 90 min. After samples were cooled to room temperature, 200 µl hexane and 1.5 ml 0.9% sodium chloride in water are added to the capped tube with shaking. After centrifuging at 1000 *g* for 1 min, the upper organic phase was transferred to a glass insert of GC vial and dried. 40 µl pyridine was added to the glass insert, 40 µl *N,O*-bis(trimethylsilyl)trifluoroacetamide (Restek, Bellefonte, PA) was added subsequently, incubated at 65°C for 2 h. Standards of 1 µl derivatized sample was injected into GCMS (Agilent 6890-5975, Santa Clara, CA), with the inlet temperature of 250°C, column helium flow of 1 ml/min, and a split ratio of 5:1. The oven temperature was held at 50°C for 1 min, raised to 200°C at the rate of 25°C/min, held at 200°C for 1 min, raised to 320°C at the rate of 10°C/min, and finally held at 320°C for 5 min. 1-Docosanol (22:0-OH), 1-eicosanol (20:0-OH), hexadecanedioic acid (16:0-DCA), 1-hexadecanol (16:0-OH), 16-hydroxy hexadecanoic acid (16:0-ωOH), C4 - C24 Even Carbon Saturated FAMEs (Sigma 49453-U), 20-hydroxy arachidic acid (20:0-ωOH) (Cayman Chemical Company, Ann Arbor, Michigan) standards were input at 2.5 µg, 5 µg, 10 µg, and 20 µg into a mixture and processed with the same procedure as the tested samples to build the standard curve. The MS spectrum of derivatized products with ±2n carbon number of these standards was calculated and identified, referring tom the retention order in (Delude et al., 2017).

Yeast One-hybrid Assay

The respective combinations of *pB42AD*-fusion effectors and *pLacZ* reporters were co-transformed to yeast strain EGY48 (Shanghai Maokang, China). Transformants were selected and grown on SD/-Trp-Ura medium. The putative interactions were observed on SD/-Trp/-Ura + X-Gal after a 3d-incubation at 30°C. Yeast transformation and growth assay were performed as described in the Yeast Protocols Handbook (BD Clontech, USA). In brief, 631 bp of the *DUF247-150* (AT3G50150) and 953 bp of the *SR3G* (At3g50160) promoter region were separately ligated into *pLacZ* vector as the reporter, while the CDS of *WRKY75* (AT5G13080) was cloned into *pB42AD* vector as the effector. The *SR3G::pLacZ* and *WRKY75-pB42AD* were transformed into the yeast strain EGY48(Shanghai Maokang, China). The respective combinations of *pB42AD*-fusion effectors and *pLacZ* reporters were co-transformed into yeast strain EGY48. Transformants were selected and grown on SD/-Trp-Ura medium. The putative interactions were observed on SD/-Trp/-Ura + X-Gal after a 3d-incubation at 30°C. Yeast transformation and liquid assay were conducted as described in the Yeast Protocols Handbook (BD Clontech, USA). The primers used for the Y1H assay are shown in **Table S4.**

Results

Natural variation in salt stress-induced changes in root:shoot ratio

To investigate salt stress-induced changes in root:shoot ratio, we developed a custom tool that quantifies green and white pixels, corresponding to shoot and root of Arabidopsis seedlings grown on agar plates (**Fig. 1**). The projected area of root and shoot showed high correlation with root and shoot fresh weight (**Fig. S1**), indicating that projected root and shoot area can be used as an accurate proxy to non-destructively measure the increase in root and shoot biomass from the images of seedlings grown on agar plates.

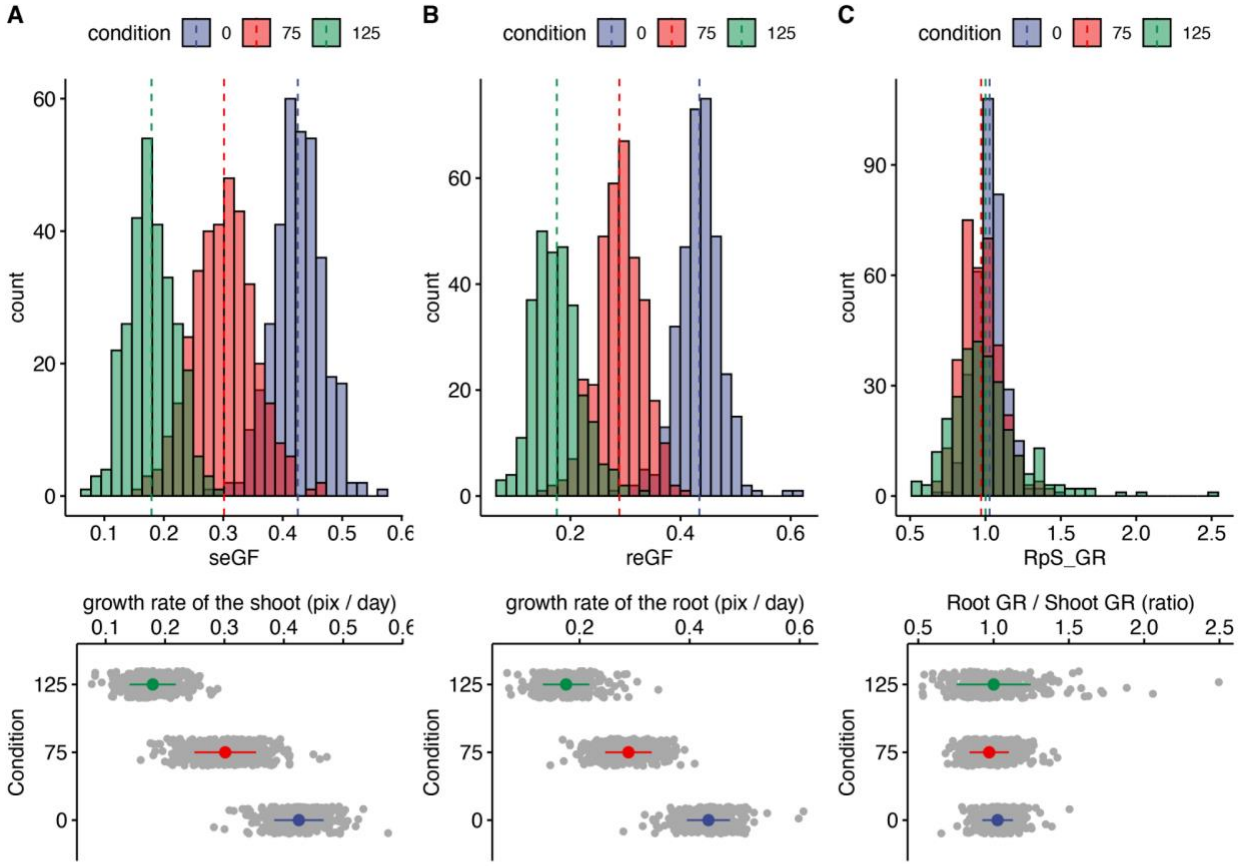

Figure 1. Salt stress is causing discoordination of root and shoot growth. Arabidopsis HapMap population was screened for salt stress-induced changes in root:shoot ratio. The increase in the projected area of shoot and root (Fig. S2) was used to estimate growth rate of **(A)** shoot and **(B)** root using an exponential function. **(C)** The root:shoot growth rate ratio was calculated per genotype. The histograms represent the number of accessions acros three studied conditions (0, 75 and 125 mM NaCl), whereas the population average is indicated using the dashed line. Additionally, the distribution of the genotypes within each treatment was additionally visualized using the error plots (lower panel), where population average and standard error is indicated using a colored point and a line respectively. Individual grey points represent individual genotypes.

Using our custom tool, we re-analyzed the data consisting of 360 Arabidopsis accessions grown on plates supplemented with 0, 75, and 125 mM NaCl (Julkowska et al. 2017), for salt stress-induced changes in the root:shoot ratio (**Fig. 1, Fig. S2**). The growth of root and shoot for each plant was estimated using the exponential function. Salt stress-induced reduction in growth rate was observed to be dose-dependent for both root and shoot (**Fig. 1A-B**). In general, the root growth was more sensitive to salt stress compared to shoot growth, with the population-wide relative growth rates reduced to a fraction of

415 0.67 and 0.41 of the growth rates observed at control for 75 and 125 mM NaCl, respectively. In
416 comparison, the growth rates of the shoot were reduced to 0.71 and 0.43 of the control in 75 and 125
417 mM NaCl treatments, respectively (**Fig. S3**). While the mean value of root:shoot growth rate did not
418 change upon salt stress treatment, the variance in the root:shoot ratio expanded with the increasing
419 concentrations of salt (**Fig. 1C**). These results suggest that while root and shoot growth are well
420 coordinated under non-stress conditions, salt stress exposure results in loss of coordination of organ
421 growth across Arabidopsis accessions. No significant correlation was found between the root:shoot
422 growth ratio and total seedling size (**Fig. S4, S5**), indicating that the relationship between coordination of
423 root and shoot growth and salt tolerance during the early seedling establishment is complex.

424 **Identification of genetic components underlying salt-induced changes in root:shoot ratio**

425 To identify genetic components underlying salt-induced changes in root:shoot ratio, we used the collected
426 data as an input for GWAS. The associations were evaluated based on the p-value, the number of SNPs
427 within the locus, and the number of traits associated with individual loci. As Bonferroni threshold differs
428 depending on the minor allele count (MAC) considered, we identified significant associations based on a
429 Bonferroni threshold for each subpopulation of SNPs based on MAC (**Table S3**). The initial GWAS was
430 performed using 250 k SNPs (Horton et al. 2012), and led to the identification of 14 significantly associated
431 loci, of which 3 and 7 loci were associated with traits measured at 75 or 125 mM NaCl treatments,
432 respectively. We identified one salt specific association on chromosome 2 (**Fig. S6**), where two SNPs were
433 identified within AT2G27300 encoding NAC-domain containing transcription factor (NTL8). Additionally,
434 salt-induced changes in root:shoot ratio and shoot:total seedling area were associated with SNPs on
435 chromosome 3, where 2 significantly associated SNPs were flanking AT3G22430, encoding an unknown
436 gene encoding a domain of unknown function (**Fig. S7**). To further prioritize the selection of candidate
437 genes for further validation study, we repeated GWAS using 4 M SNPs (1001 Genomes Consortium.
438 Electronic address: magnus.nordborg@gmi.oeaw.ac.at and 1001 Genomes Consortium 2016). Increased
439 SNP density GWAS revealed 32 additional loci, with only one significantly associated locus being picked
440 up by both 250k and 4M SNPs GWAS (locus 30, **Table S3**). We further prioritized the identified associations
441 based on the number of significantly associated SNPs, minor allele count (MAC), and number of traits
442 associated with each locus, and identified three loci of major interest (**Table S4**). The region within linkage
443 disequilibrium (LD) of the significantly associated SNPs was investigated for the sequence divergence and
444 open reading frames (**Fig. 2, Fig. S8, Fig. S9**).

445 Out of identified associations, locus 30 stood out as it consisted of nine SNPs associated with p-
446 value above the Bonferroni threshold, and was associated with both root:shoot and shoot:total seedling
447 area at 6 and 8 days after transfer of the seedling to 125 mM NaCl (**Fig. 2A-B, Fig. S8, Table S4**). The
448 significantly associated SNPs were located in and around the gene coding region of AT3G50160, which
449 encodes a domain of unknown function 247 (DUF247). We investigated the region for sequence
450 divergence, and found that the region contained not only a high degree of sequence diversity but also
451 potential structural variants (**Fig. 2C**). To identify allelic variation underlying the initial associations, we
452 performed haplotype analysis, where accessions with shared SNP pattern within the protein-coding part
453 of AT3G50160 were grouped into individual haplotype-groups (**Fig. 2D**). Each unique haplotype,
454 represented by at least three accessions, was subsequently studied for differences in observed
455 phenotypes. We observed that Haplotype 1, represented by 46 accessions including Col-0, was
456 significantly different from Haplotype 11, represented by 11 accessions including Blh-1, in shoot-per-total
457 seedling area at 6 days after transfer to 125 mM NaCl (**Fig. 2D**), as well as shoot growth rate and relative
458 shoot growth rate at 125 mM NaCl (**Fig. S9**). Upon further investigation and sequencing of AT3G50160 in
459 both Col-0 and Blh-1 accessions, we discovered that the Blh-1 allele carries a large insertion at 644
460 nucleotides downstream from the ATG of AT3G50160, followed by multiple other sequence variations
461 (**Fig. S10**). The first insertion leads to a premature STOP-codon within the DUF247 domain after Gly-215

462 (**Fig. 2E, Fig. S11**), resulting in a truncated protein that still carries a nuclear localization signal and coiled-
463 coil domain, but is missing a major part of the calcium-binding domain and a predicted transmembrane
464 domain (**Fig. S12**). As there are other DUF247s within the locus associated with salt-induced changes in
465 root:shoot ratio, we decided to name the gene containing majority of the associated SNPs (At3g50160) as
466 Salt Root:shoot Ratio Regulator Gene (SR3G). Together, these results suggest that the allelic variation in
467 SR3G protein sequence might underlie the observed differences in root:shoot ratio under salt stress
468 conditions.

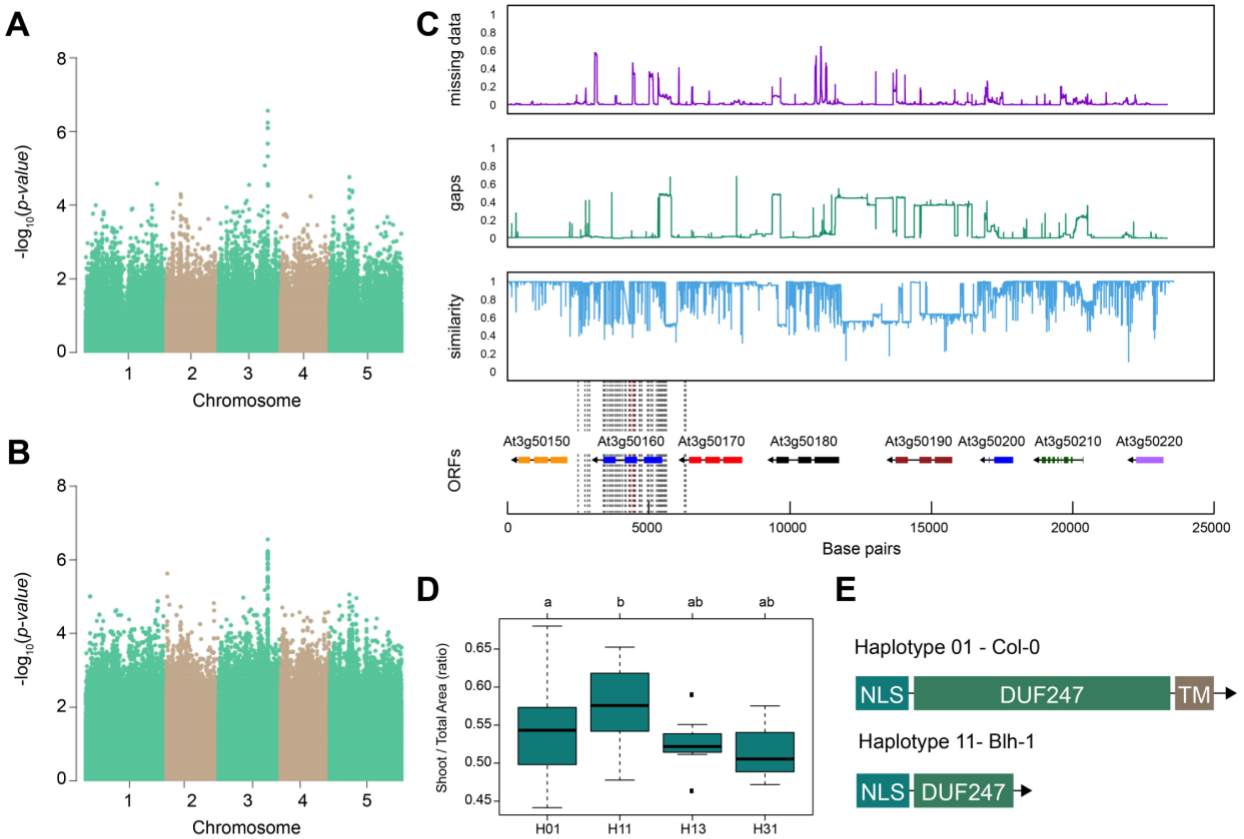

Figure 2. SR3G is associated with salt stress-induced changes in shoot-per-total seedling area ratio. The salt induced changes in root-to-shoot and shoot-per-total seedling area ratios were used as an input for GWAS. Manhattan plots representing the associations of shoot-per-total seedling area recorded 6 days after transfer to 125 mM NaCl and **(A)** 250 k SNPs and **(B)** 4 M SNPs. **(C)** Significant associations were found with the SNPs forming a locus on chromosome 3 in and around SR3G (AT3G50160), encoding Domain of Unknown Function 247 (DUF247). The natural variation in the LD region was studied in 162 accessions sequenced by 1001 Genomes Project. The upper panel represents portion of the missing data, upper middle panel represents deletions relative to Col-0, while lower middle panel represents the sequence similarity compared to Col-0. The bottom panel represents the open reading frames (ORFs) within the LD, and the location of associated SNPs is indicated with the dashed lines. Red dashed lines represent associations above Bonferroni threshold in 250k SNP mapping, while grey lines represent associations with -log10(p-value) > 5 in the 4M SNP mapping. **(D)** The haplotype analysis performed using SNPs located within the coding region of the SR3G revealed significant differences in shoot-per-total seedling area recorded 6 days after transfer to 125 mM NaCl between Haplotype groups 1 (represented by 46 accessions, including Col-0) and 11 (represented by 11 accessions, including Blh-1). The significant differences between individual haplotype groups were tested using ANOVA with Tukey HSD to identify significantly different groups. **(E)** Upon further sequencing of SR3G in accessions from Haplotype 1 and 11, revealed two 200 bp insertions within SR3G exons in 4 tested accessions belonging to haplotype 11 group. These 200 bp insertions resulted in a premature STOP-codon within the DUF247 domain (after Gly-215).

469

470 **Evolutionary context of SR3G locus reveals its origin in local genome duplication**

471 SR3G sits in what appears to be a tandemly duplicated array of DUF247s along Arabidopsis chromosome
472 3. The genome-wide identification of SR3G included eight DUF247 paralogs, AT3G50120, AT3G50130,
473 AT3G50140, AT3G50150, AT3G50170, AT3G50180, AT3G50190, and AT3G50200. Reciprocal best BLAST
474 within CoGe's BLAST tool of these nine DUF247 paralogs against the genomes of seven other Brassicaceae
475 (see **Table S5**) revealed a total of 50 potential orthologs used for downstream analysis. While the copy

476 number of DUF247 loci are similar across the examined species, the noted exceptions are those with
477 recent whole genome duplication events (*Brassica rapa* and *Camelina sativa*). Given these data, it appears
478 that DUF247 loci are commonly tandemly duplicated, although the eight paralogs observed in Arabidopsis
479 represents an extreme case for this gene family.

480 To examine conservation within the predicted DUF247 functional domains, we generated an
481 amino-acid based multiple sequence alignment using MUSCLE. All of the identified DUF247 proteins
482 contained the DUF247 domain near the center of the translated sequence. While partial deletions were
483 identified outside of the DUF247 domain at the C-terminus of a few DUF247s, such as *CARHR159180*,
484 *Csa09g052970*, and *Bra01902*, in general the DUF247 domains were highly conserved across Brassicaceae.
485 The amino acid sequences spanning the "coiled-coil domain" (Amino acid position: Met153-Lys173),
486 putative Ca^{2+} binding domain (Amino acid position: Gly210-Phe372), and super polar fragment (Amino
487 acid position: Ser301-Ile320) were further selected for phylogenetic reconstruction (**Fig. 3B**). The resulting
488 phylogeny demonstrated that SR3G is sister to a clade containing AT3G50150 and representatives from
489 *C. sativa*, *Capsella rubella,* and *A. lyrata*, with representative DUF247s from *B. rapa* and
490 *Eutrema salsugineum* serving as a monophyletic outgroup. These data support a hypothesis where SR3G
491 is a recent duplicate (likely A/C Clade specific; (Forsythe, Nelson, and Beilstein 2020)) of AT3G50150 and
492 that representative SR3G sequences in *C. sativa*, *C. rubella*, and *A. lyrata* have been lost.

493 Given the specific retention of AT3G50150 in *A. thaliana*, we next tested whether this locus is
494 experiencing selection. To test this assumption, we grouped the branches leading to SR3G into four groups
495 (**Figure 3B**: ω0, ω1, ω2, and ω-rest) and then performed a branch-site model A hypothesis test**.** In our null
496 hypothesis (H_0), we hypothesized that all branches have the same selection pressure (H_0: ω -rest branches
497 = ω0 = ω3 = ω1 = ω2). For our alternative hypothesis, we created five different ω groups to cover scenarios
498 where specific branches may be experiencing selection (See Methods). Based on our analysis, the branch
499 leading to SR3G is experiencing selection (likelihood score = 20625.5, Chi-square derived P value; P =
500 0.00418). Interestingly, no other branches appeared to be experiencing selection. To pinpoint specific
501 amino acids within SR3G under selection, we performed the Bayes Empirical Bayes (BEB) test, identifying
502 three sites with a posterior probability > 0.90, including 124C (P = 0.992), 206A (P = 0.951), and 209A (P =
503 0.988). Two out of three sites are located at the putative Ca^{2+} binding site and all three sites possess a

504 unique amino acid compared with the other 49 amino acid sequences (**Fig. 3C**).

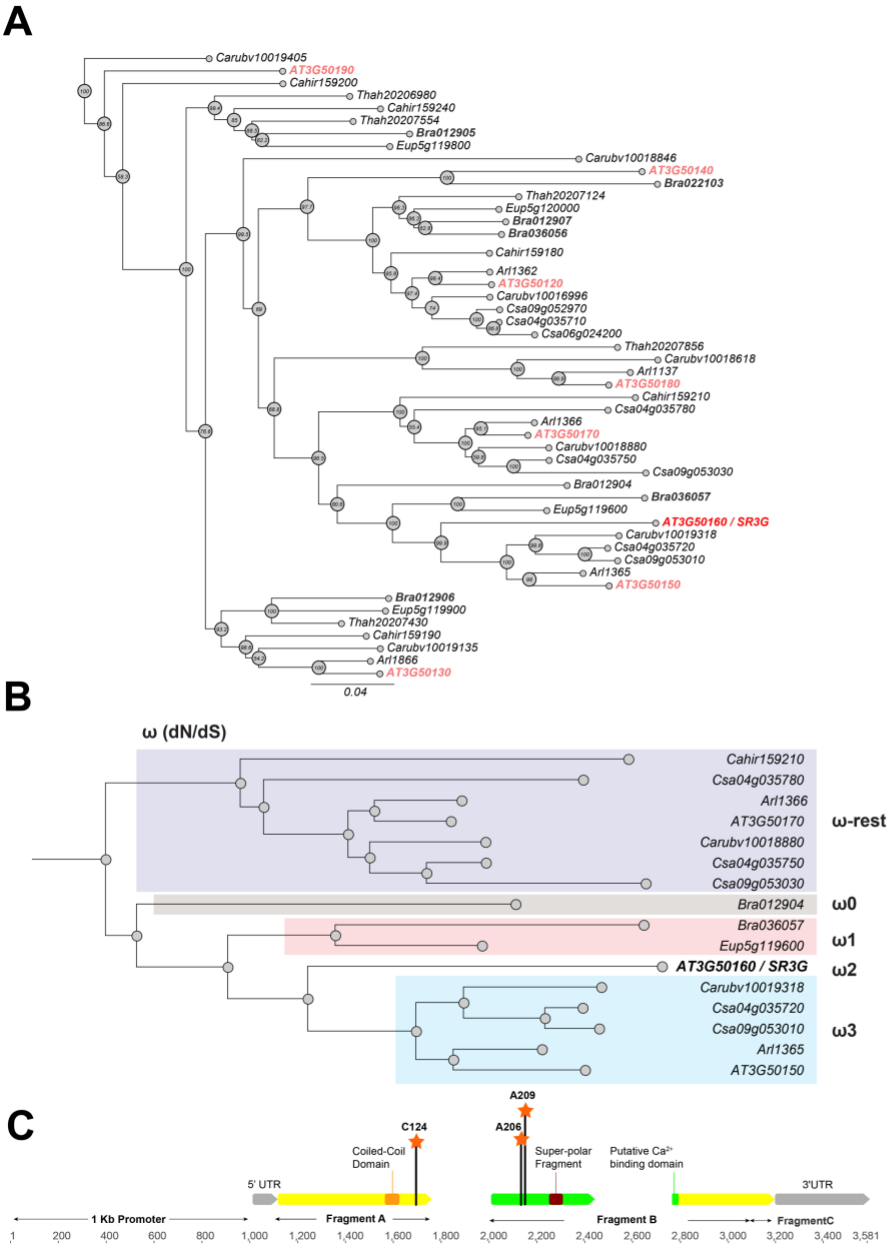

Figure 3. Phylogeny and positive selection analysis of SR3G and its orthologs from other species. The orthologous genes of SR3G (AT3G50160) from other seven species were identified using GoGeBlast (E-value < 1.00E-10). **(A)** The protein sequences of the 50 homologous genes were aligned by MUSCLE and then an unrooted phylogenetic tree was reconstructed by a Maximum -likelihood (ML)-derived style by RAxML (Bootstrap number: 100). **(B)** A positive selection analysis was conducted by branch-site model A test: Specifically, we hypothesized the differential or constant dN/dS (ω) substitution rate among the closely distant branches leading to DUF247 (AT3G50160) (See Method & Materials for details). These branches were marked as ω1 (light brown branch), ω2 (DUF247-specific branch), ω3 (light blue branch), and ω-rest (light purple branch). **(C)** The gene structure of DUF247 (AT3G50160) was illustrated by wide arrows (grey arrow: 5 and 3' UTR, yellow arrow: coding-region). The regions used for cloning (Fragment A, B, and C) were marked by narrow arrows along with "Coil-Coil Domain", "Putative Ca2+ binding fomain" and "Super-polar Fragment" marked on Fragment A and B, respectively. Lastly, the Bayes Empirical Bayes (BEB) was performed to test the probability of sites along with ω > 1 over the DUF247 (AT3G50160). Three sites were generated with a posterior probability > 0.90: 124C (P = 0.992), 206A (P = 0.951), and 209A (P = 0.988). These three sites were marked with an orange asterisk and assumed to have been undergoing positive selection.

505

506 ***SR3G* expression is enhanced in root by salt stress**

507 To identify the developmental window and specific plant tissues where *SR3G* gene is active, we examined
508 its expression pattern. Based on Arabidopsis eFP Browser (http://bar.utoronto.ca/), *SR3G* expression is
509 relatively low, and restricted to the early stages of seedling development (**Fig. S13A**). Upon examining
510 the expression profiles specific to different tissues, we observed that *SR3G* is predominantly expressed in
511 the root stele (**Fig. S13B**). Moreover, *SR3G* expression was induced by salt stress (**Fig. S13C**). To validate
512 these results, we performed RT-qPCR on 11 days old seedlings of Col-0 exposed to 0 or 75 mM NaCl for 7
513 days. In Col-0 seedlings, the transcript levels of *SR3G* were higher in shoot compared to the root tissue
514 (**Fig. 4A**). Interestingly, the *SR3G* transcripts increased only in root (54 folds) upon salt stress exposure but
515 not in shoot (**Fig. 4A**). These results suggest that *SR3G* has a root-specific function in the salt stress.

We further examined expression profiles of other *DUF247* genes that directly neighbor *SR3G* in response to salt stress using the eFP Browser. We observed similar expression patterns as *SR3G* for other *DUF247s* including At3g50150, indicating their responsiveness to salt stress (**Fig. S14**). Because *DUF247-150* (At3g50150) is closely located to the *SR3G* in chromosome 3, we investigated its gene expression in young seedlings. We observed that its expression was higher in shoot compared to the root tissue. However, its expression remained unchanged in both root and shoot under salt stress (**Fig. 4B**). For the remaining *DUF247* genes (At3g50120 and At3g50200), we observed no significant changes, while others (At3g50130, At3g50140, At3g50170, At3g50180) showed reduced expression upon exposure to salt stress (**Fig. S14**). These results suggest that *SR3G* is the main gene involve in regulation of root development under salt stress.

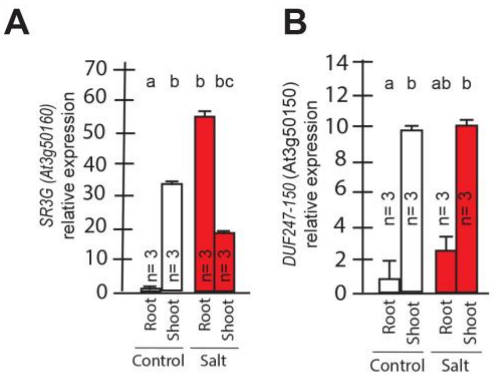

Figure 4. Transcript abundances for the two closely related DUF247s. Expression of **(A)** SR3G (AT3G50160) **(B)** and its closest homologue DUF247-150 (AT3G50150) were measured in Col-0 seedlings grown with and without salt stress. RT-qPCR analyses were conducted using seedlings grown on 1/2x MS for 4 d and then followed by transferring to the treatment plates with or without 75 mM NaCl for one week. Mean values are shown ± SE, with number of replicates (n) shown in each graph. AT4G04120 was used as a reference gene for normalization. Significance was determined by the Tukey–Kramer HSD test in JMP.

SR3G relocates from plasma membrane to nucleus/cytosol after removal of its transmembrane domain

SR3G protein is predicted to contain a nuclear localization signal (Lys15-Ala19), a coiled-coil domain (Met153-Lys173), a $Ca2^{+}$ binding pocket (Gly210-Phe372), and a trans-membrane domain (Pro469-Thr503) (**Fig. S15**). We generated constitutive expression constructs of full-length *SR3G* gene CDS, and a combination of individual domains (refer to as A, B, and AB domains) to identify their subcellular localization (**Fig. S15**). Fragment A comprised a nuclear localization signal, a coiled-coil domain, and the initial segment of the Ca^{2+} binding pocket, encompassing seven amino acids. Fragment B encompassed the remaining segment of the Ca^{2+} binding pocket. Fragment C only included the transmembrane domain. All constructs contained N-terminal fusion of mVenus. The individual constructs were used in transient expression assay in tobacco leaves. Our result showed that full-length SR3G localizes to the plasma membrane (**Fig. 5A**) as its signal overlapped with FM4-64, the plasma membrane marker (**Fig. 5B**). The SR3G fragments from which the transmembrane domain was excluded—namely fragments A, B, and AB—exhibited localization in both the nucleus and cytosol, resembling the pattern observed with free-GFP localization (**Fig. 5C-F**). It is noteworthy that while the signal from fragment A was directed to both the cytosol and nucleus, its intensity was notably stronger in the nucleus (**Fig. 5C**), aligning with the prediction that it contains the nuclear localization signal. Together, these findings indicate that the positioning of SR3G within the plasma membrane is due to the transmembrane domain encoded within the fragment C, and its removal could potentially release the protein into both the nucleus and cytosol.

552

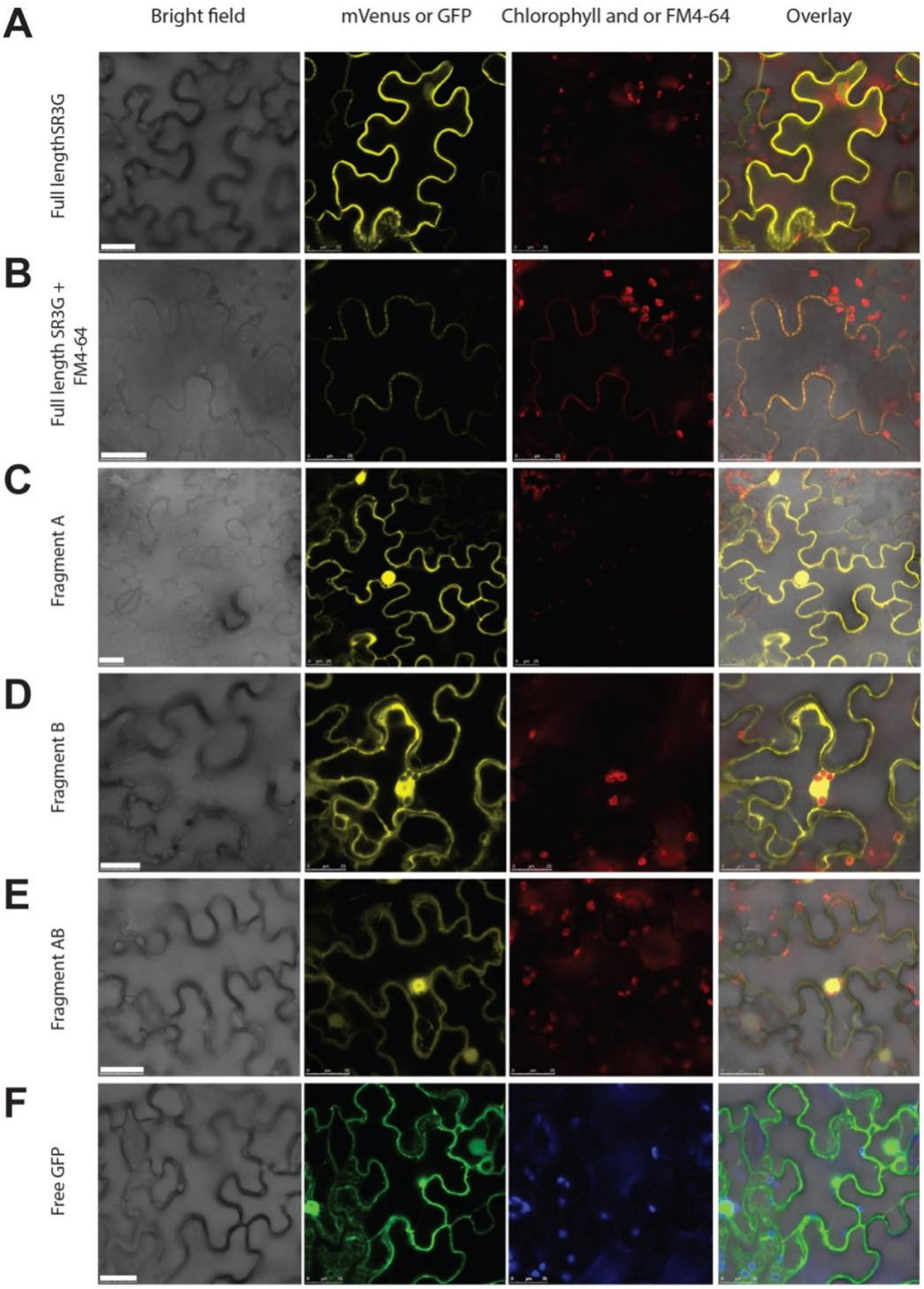

Figure 5. SR3G full-length protein resides in the plasma membrane while removal of its transmembrane domain results in protein relocation to nucleus and cytosol. SR3G full-length protein **(A-B)** or truncated versions **(C-E)** fused to mVenus at the N-terminus were agro-infiltrated into the Nicotiana benthamiana leaves for transient expression. Shown are a bright-field image of transfected leaf cells and mVenus-SR3G-mediated fluorescence as well as GFP-based subcellular marker. (A) Localization of full-length SR3G alone or (B) in combination with the known plasma membrane dye, FM4-64. Localization of truncated versions of SR3G are shown for (C) SR3G-Fragment A, (D) SR3G-Fragment B, and (E) SR3G-Fragment AB. (F) Free GFP was used as a nuclear and cytosolic marker. Scale bar = 25 µm.

553 **Lower expression of *SR3G* results in reduced lateral root development under salt stress**

554 To investigate role of *SR3G* in salt-induced changes in root growth and development, we studied the root
555 system architecture of two T-DNA insertion lines: *sr3g-4* (SAIL_690_E12) and *sr3g-5* (SAIL_608_C06)
556 localized in second exon and first intron region of the *SR3G* gene, respectively (**Fig. S16A**). Among these
557 two mutant lines, *SR3G* expression was significantly reduced in the *sr3g-5* mutant compared to Col-0 (**Fig.**
558 **S16B**), indicating the *sr3g-5* is a knockdown mutant. We did not observe any differences in *SR3G* transcript
559 abundance between *sr3g-4* and Col-0 (**Fig. S16B**). Moreover, we examined the transcript abundance of
560 the closely related gene (i.e., *DUF247-150, At3g50150*) in the *sr3g-5* mutant, and found no significant
561 difference. In the case that *DUF247-150* would act redundantly to *SR3G*, we would expect that the
562 expression of *DUF247-150* would be increased in *SR3G* knockdown mutant. As this is not the case, these
563 results further contribute to the evidence that *SR3G* and *DUF247-150* are not acting redundantly (**Fig.**
564 **S16C**).

565 Two T-DNA insertion lines were subsequently studied for salt-induced alterations in root
566 architecture (**Fig. 6 and Fig. S17 and S18**). Among the various features of the root system architecture that
567 we investigated (**Fig. S17**), *sr3g-5* exhibited a significantly reduced growth rate of lateral roots under 75
568 mM NaCl, but not under 125 mM NaCl, when compared to Col-0 (**Fig. 6A**). Likewise, the *sr3g-5* mutant
569 displayed a significant reduction in the Stress Tolerance Index (STI), calculated as the ratio of growth rate
570 under salt to growth rate under control conditions, for lateral root length under 75 mM NaCl (**Fig. 6B**). No
571 significant difference was observed between *sr3g-4* and Col-0 (**Fig. S18**), except for Stress Tolerance Index
572 (STI) calculated using growth rates of lateral root length and number, consistent with the observations
573 made for the *sr3g-5* mutant line (**Fig. 6B).** Based on the RT-qPCR results (**Fig. S16**), we proceeded to further
574 investigate the role of *SR3G* in salt stress, focusing on the sr3g-5 mutant in our subsequent investigations.

575 As Na^+ exclusion from the shoot is one of the main mechanisms of salt tolerance (Munns and
576 Tester 2008; Møller et al. 2009; Julkowska et al. 2017), we further investigated the role of *SR3G* in ion
577 exclusion using plate-grown seedlings. We used root and shoot samples collected for Col-0 and *sr3g-5*
578 mutant to examine Na^+ and K^+ accumulation using ICP-AES at 14 days after exposure to salt stress. While
579 salt stress increased Na^+ and decreased K^+ in all studied samples (**Fig. S17**), we observed no significant
580 differences between Col-0 and *sr3g-5* mutant for Na^+ and K^+ accumulations and their corresponding ratio
581 (**Fig. 6C**). These results suggest that *SR3G* plays a role in root development under the salt, but does not
582 affect ion accumulation at early developmental stages.

583 To evaluate the effects of other closely related DUF247 genes on root development, we have
584 investigated the T-DNA insertion lines targeting the neighboring DUF247 genes (AT3G50120, AT3G50130,
585 AT3G50140, AT3G50150, AT3G50170, AT3G50180, AT3G50190, AT3G50200), and RNAi lines targeting
586 one or more DUF247s within the interval (**Table S4, Fig. S19-S23**). For the screened T-DNA insertion lines
587 (**Fig. S19-20**), we have not observed consistent changes in main or lateral root development in either
588 control or salt stress conditions across alleles targeting the same gene. The only exception was *DUF247-*
589 *200* encoded by AT3G50200, where two out of three studied T-DNA insertion alleles exhibited increased
590 salt tolerance index for main root growth rate (**Fig. S20**).

591 For the screened RNAi lines (**Table S4, Fig. S21-S23**), we observed the most interesting root
592 architecture phenotypes in lines targeting the neighboring genes of the *SR3G* (RNAi line #04, targeting
593 AT3G50150, RNAi line #16 targeting AT3G50130, *SR3G*, and AT3G50170, and RNAi line #19 targeting
594 AT3G50130, AT3G50140, AT3G50150, *SR3G*, AT3G50170, AT3G50180, and AT3G50190). Three out of five
595 screened independent transformation lines from RNAi line #04 showed a decreased relative main root
596 length (Salt / Control, CSHL #4 B2a, D4a, and G1d), whereas two lines showed a decrease in relative lateral
597 root number (CSHL #4 D4a and F1b), and one line showed decreased lateral root length at 75 mM NaCl
598 (CSHL #4 D4a **Fig. S21-23**). Two out of two independent transformants for RNAi line #16 showed a
599 decreased relative main root length and increased lateral root number at 75 mM NaCl (CSHL #16 A2c and

B1a, **Fig. S21-23**). In three of the four screened independent transformants of line #19 we observed an increased lateral root length at 75 mM NaCl (CSHL #19 F1a, I3c, and L1c **Fig. S21-23**). We did not observe strong reduction in lateral root development across RNAi lines targeting two closely related DUF247 genes (i.e., RNAi line #22, targeting AT3G50150 and *SR3G*), as in the single mutant (**Fig. 6, Fig. S21**). The above results further support that these two genes do not act redundantly in the context of lateral root development.

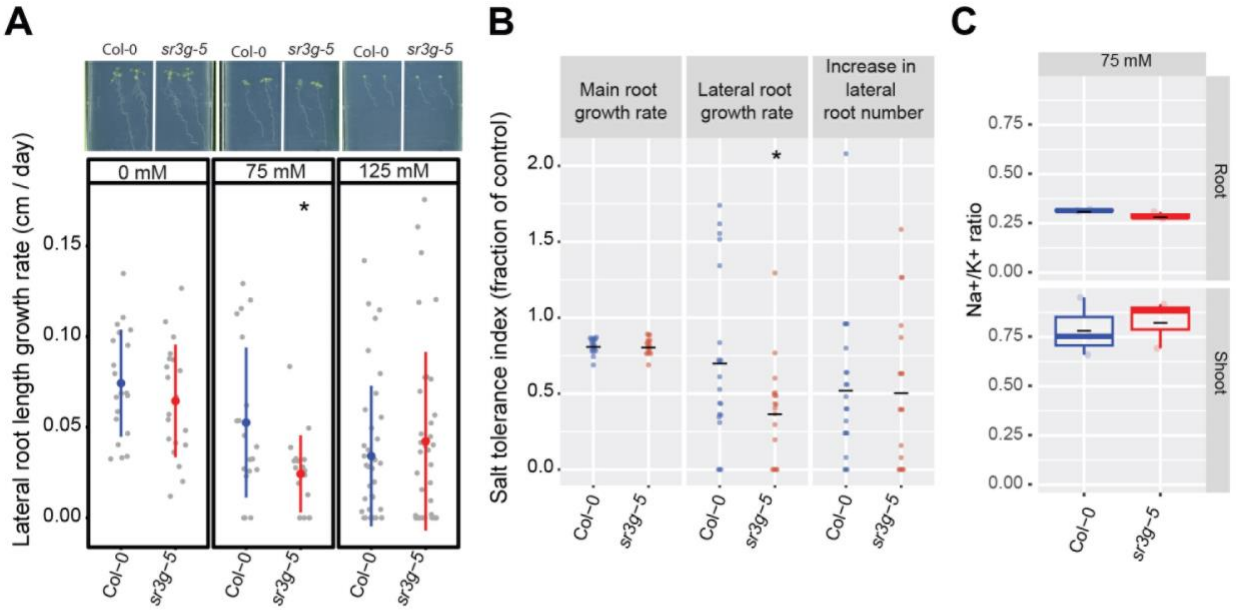

Figure 6. sr3g mutant displays reduced growth rate for the lateral root length and Na+ content in the root. Root system architecture analysis of Col-0 and sr3g-5 genotypes under various concentrations of NaCl are shown here. **(A)** Shown are representative images of 13-day-old Col-0 and sr3g-5 genotypes that experienced 9 days of salt treatment at indicated concentrations as well as growth rate for lateral root length. **(B)** Salt Tolerance Index (STI) for the main root length, average lateral root length, and lateral root number at 75 mM NaCl. The STI was calculated by dividing the growth rate measured under salt stress by the growth rate measured under control condition for each genotype. **(C)** Na^+/K^+ ratio in root and shoot of Col-0 and sr3g-5 after two weeks on 75 mM salt are shown. Each dot in (A) and (B) represents individual replicate per genotype. Lines in (A) and (B) graphs represent median and average, respectively. In (A) and (B), the asterisks above the graphs indicate significant differences between Col-0 and the sr3g-5 mutant, as determined by the Student 's t-test: *P < 0.05. Statistical analysis in (C) was done by comparison of the means for all pairs using Tukey–Kramer HSD test. Levels not connected by the same letter are significantly different (P < 0.05). Root system architecture and ICP-AES analyses of Col-0 and sr3g-5 mutant are shown in details in Figure S17.

Loss of *SR3G* results in increased salt tolerance in soil

To investigate *SR3G's* contribution to salt stress tolerance beyond seedling stage and agar plate conditions, we evaluated the performance of Col-0 and *sr3g-5* mutant in soil. We exposed the soil-grown plants to salt stress and imaged the rosette size every 30 minutes for two weeks using the automated imaging platform (L. 'ang Yu et al. 2023). As salt-induced changes depend on the developmental stage at which the stress is applied (Julkowska et al. 2017), we examined the role of *SR3G* exposed to salt stress at 2 or 3 weeks after germination, corresponding to early and late vegetative stages. We calculated a daily growth rate for each plant, using the projected rosette area. No significant difference was observed between Col-0 and *sr3g-5* mutant under control conditions (**Fig. 7A-B**), indicating that *SR3G* does not play a role in plant development under non-stress condition. Significant difference was observed between Col-0 and *sr3g-5* for plants exposed to early salt treatment (**Fig. 7A-B**), where *sr3g-5* mutant displayed an

619 increased rosette growth rate as compared to Col-0 (**Fig. 7A**). Late stress exposure resulted in significantly
620 higher *sr3g-5* growth rate at two and three days after exposure to salt stress (**Fig. 6A**). Similarly, the *sr3g-*
621 *5* mutant showed a significantly higher rosette area compared to Col-0 exclusively when plants were
622 exposed to salt stress at an earlier stage of their development (**Fig. 7A**).
623 To investigate the role of *SR3G* in the maintenance of cellular integrity during salt stress, we
624 evaluated the salt-induced changes in cell membrane integrity by measuring ion leakage in the leaf discs
625 at the end of the experiment (**Fig. 7C**). While ion leakage increased significantly in Col-0 under early salt
626 stress conditions, no salt-induced change was observed for *sr3g-5* compared to control condition (**Fig. 7C**).
627 Although the *sr3g-5* mutant exhibited increased ion leakage in response to late salt stress, this
628 phenomenon may be more closely associated with the onset of senescence rather than direct exposure
629 to salt stress (**Fig. 7C**).
630 We further explored the role of *SR3G* in ion exclusion by quantifying the accumulation of Na^+ and
631 K^+ ions in the rosette at the end of the experiment (4-weeks-old plants). We observed a reduced
632 accumulation of Na^+ in *sr3g-5* mutants compared to Col-0 for plants exposed to salt stress at an earlier
633 timepoint (**Fig. 7D**). No significant differences in Na^+ accumulation was observed between the Col-0 and
634 *sr3g-5* at the late salt stress regime (**Fig. 7D**). A subtle, non-significant, reduction in K^+ content was
635 observed in *sr3g-5* mutant compared to Col-0 across all three conditions studied (**Fig. 7E**). In summary,
636 these results suggest that *SR3G* plays a negative role in maintenance of plant growth, cellular integrity
637 and Na^+ accumulation during the salt stress, especially when the salt stress is applied during early
638 vegetative development.

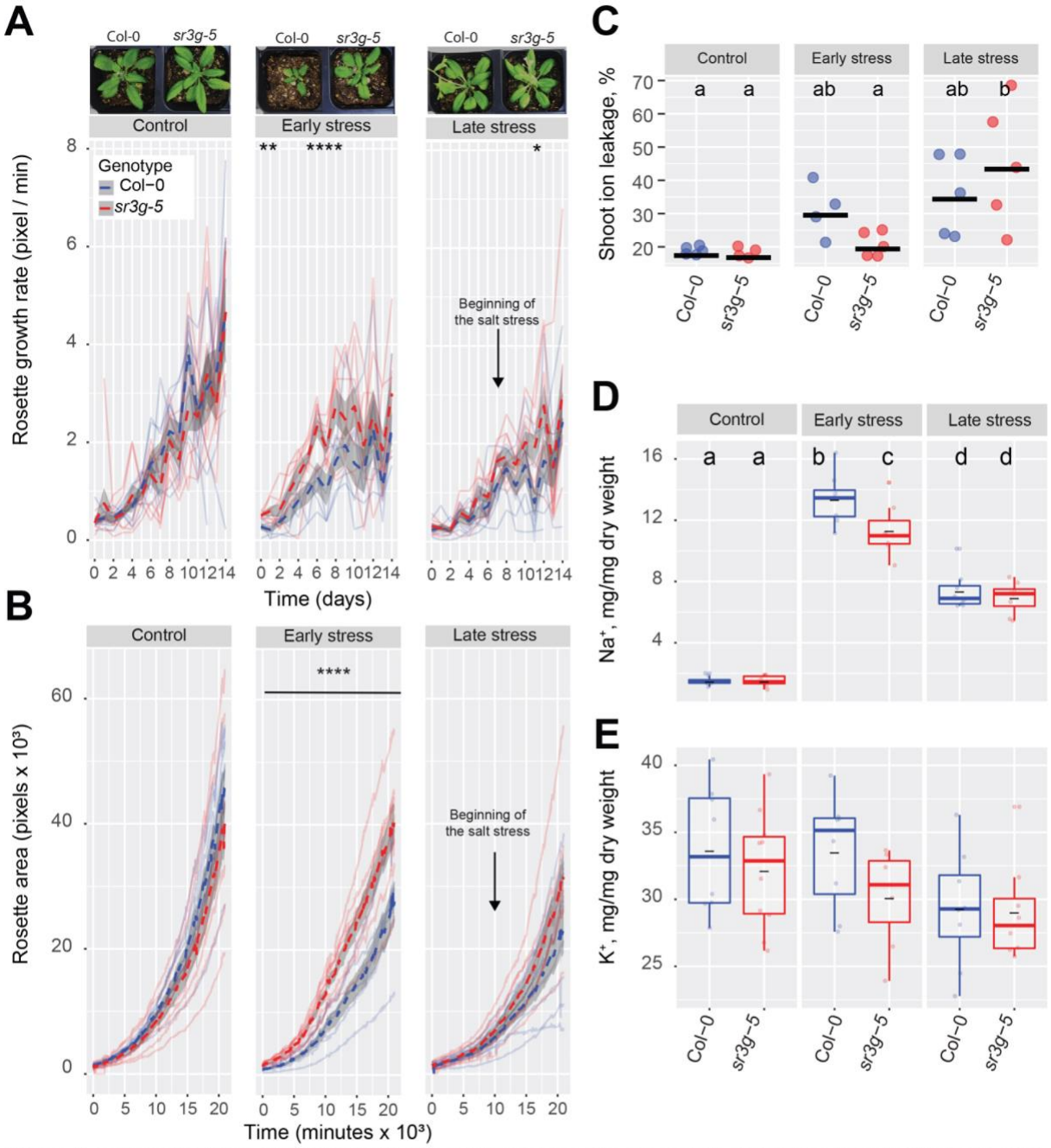

Figure 7. sr3g mutant has higher growth rate and larger rosette area while displaying less ion leakage and Na+ accumulation in shoot under salt stress. The salt stress responses of 2-week-old (referred to as "early salt stress") or 3-week-old (referred to as "late salt stress") soil-grown Col-0 and sr3g-5 plants that were exposed to a final concentration of 100 mM NaCl were examined here. **(A)** Rosette growth rate and **(B)** area were monitored over a period of two weeks, during which the "early salt stress" group experienced two weeks of salt stress while the "late salt stress" group experienced one week. Representative images of 4-week-old Col-0 and sr3g-5 genotypes were shown in (A). **(C)** Ion leakage percentage, **(D)** Na^+ and **(E)** K^+ contents in shoot were measured in 4-week-old plants. Each line in (A) and (B) represents the trajectory per genotype through time, where red and blue lines indicate Col-0 and sr3g-5 plants grown under control or salt-stress conditions, respectively. The dashed lines represent the mean values of the genotype per condition, whereas the grey band represents the confidence interval. The asterisks above the graphs indicate significant differences between Col-0 and sr3g-5 plants, as determined by one-way analysis of variance: *P < 0.05, **P < 0.01, ***P < 0.001, and ****P < 0.0001. Statistical analysis in (C) to (E) was done by comparison of the means for all pairs using Tukey–Kramer HSD test. Levels not connected by the same letter are significantly different (P < 0.05).

640 ***sr3g* mutant displays enhanced root suberization**

641 As *SR3G* limits shoot growth, promotes cell damage and sodium translocation into shoot (**Fig. 7**), and is
642 expressed in the most inner layers of the root (i.e., stele, **Fig. S13**), we hypothesized that *SR3G* plays a role
643 in the regulation of suberization within the Casparian strips located in the endodermis, the layer adjacent
644 to the stele. Salt stress exposure increases root suberization, thereby limiting Na^+ loading into the
645 transpiration stream and accumulation in the shoot (Baxter et al. 2009). We examined root suberization
646 patterns in Col-0 and *sr3g-5* under non-stress and salt stress conditions. Root suberization was visualized
647 using lipophilic stain Fluorol Yellow (FY), and staining intensity was examined under a confocal
648 microscope. Additionally, we examined the developmental transition in root suberization through imaging
649 four regions along the main root (**Fig. 8**). Visually, we observed that roots of *sr3g-5* were more suberized
650 compared to Col-0 under both control and salt stress conditions (**Fig. 8A**). The quantification of FY signal
651 intensity revealed higher levels of root suberization in *sr3g-5* compared to Col-0 in sections one to three
652 of the root under control condition (**Fig. 8B**). Only in root section four, the level of suberization
653 significantly decreased in *sr3g-5* compared to Col-0 (**Fig. 8B**). In plants exposed to salt stress, we observed
654 a non-significant difference between *sr3g-5* and Col-0 throughout the four sections, although, in section
655 one which is the root tip proximal, *sr3g-5* showed more suberization compared to Col-0 (section 1, **Fig.**
656 **8A**). These results suggest that *SR3G* may play a negative role in root suberization.

657 To validate the FY histochemical analysis, we quantified root suberin monomers in the Arabidopsis
658 seedlings using GC-MS analysis. Suberin monomers that were detected in the Arabidopsis roots included
659 fatty acid (FA), fatty alcohol (OH-FA), α,ω-dicarboxylic acids (DCA), and ω-hydroxy fatty acid (ωOH-FA).
660 Roots of *sr3g-5* contained significantly more total FA and DCA monomers compared to Col-0 under control
661 condition, whereas the total OH-FA and ωOH-FA remained unchanged (**Fig. 8C**). In plants exposed to salt
662 stress, the *sr3g-5* mutant showed an increased abundance of three suberin monomers, with DCA and
663 ωOH-FA showing the most significant changes (**Fig. 8C**). The total FA decreased significantly in the mutant
664 compared to Col-0 (**Fig. 8C**). Together, these results further corroborate with FY staining, suggesting that
665 SR3G plays a negative role in root suberization.
666
667

668

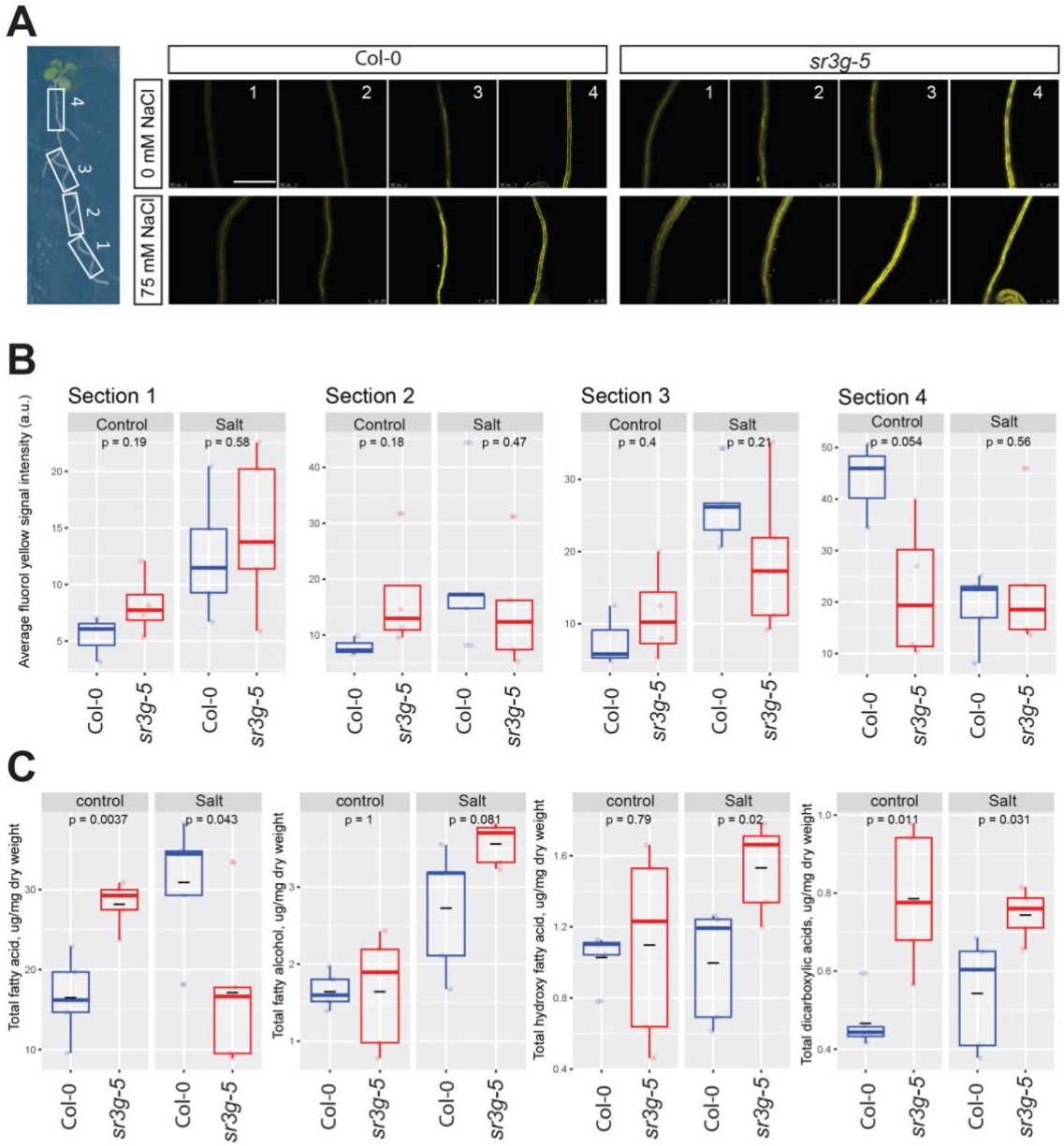

Figure 8. sr3g mutant root is more suberized than Col-0. (A) Representative images of fluorol yellow (FY) staining of four root sections (# 1 to 4, from root tip to root base as shown by white rectangles across the seedling) were shown for Col-0 and sr3g-5 mutant with or without 75 mM NaCl. Seeds were germinated on the 1/2 MS plates for 4 d and then seedlings were transferred to the treatment plates with or without 75 mM NaCl for 2 more days. **(B)** Quantification of FY signal intensity for each root section. The FY quantification was done using ImageJ. Scale bar is equal to 500 µm in all. **(C)** Suberin monomers detected using Gas Chromatography–Mass Spectrometry (GC-MS) in the Col-0 and sr3g-5 mutant roots with or without 75 mM NaCl included fatty acid (FA), fatty alcohol (OH-FA), α,ω-dicarboxylic acids (DCA), and ω-hydroxy fatty acid (ωOH-FA). The significant differences between Col-0 and sr3g-5 mutant were evaluated using Student 's t-test.

669 ***SR3G* expression is regulated by *WRKY75* transcription factor**

670 To identify potential transcriptional regulators of *SR3G*, we examined the *SR3G* promoter for cis-
671 regulatory elements using the CisCross tool (https://plamorph.sysbio.ru/ciscross/), and made a list of
672 transcription factors that putatively interact with *SR3G* promoter (**Fig. 9A**). As the root stele showed the
673 highest enrichment in the *SR3G* transcript (**Fig. S13**), we examined the transcription factors that were
674 previously identified to be expressed in root stele (Brady et al. 2011). Cross-referencing of these two
675 datasets revealed one transcription factor, *WKRY75* (AT5G13080) that was both enriched in root stele,
676 and potentially binding to *SR3G* promotor.

677 *WRKY75* was previously described to act as a positive regulator of salt stress response by
678 enhancing *SOS1* expression (Lu et al. 2023). To investigate whether the *SR3G* expression depends on
679 *WRKY75*, we examined the *SR3G* expression in the *wkry75* T-DNA insertion lines. *SR3G* expression was
680 undetected in *wrky75* loss-of-function mutants (**Fig. 9B**), suggesting that *WKRY75* regulates *SR3G*
681 expression. In comparison, expression of *WRKY75* remained unchanged in the *sr3g-5* mutant when
682 compared to Col-0 (**Fig. 9C**). To investigate whether *WRKY75* directly binds to the *SR3G* promoter, we
683 performed Y1H assay. Similar to the two positive controls, the strains transformed with WRKY75-AD and
684 SR3G:pLacZ grew on the SD/-Trp/-Ura + X-Gal medium, thereby confirming the interaction between
685 *WRKY75* and *SR3G* promoter region (**Fig. 9D**). In contrast, *WRKY75* did not show binding affinity to the
686 promoter region of the adjacent gene to the *SR3G* (i.e., DUF247-150, AT3g50150), thereby reinforcing the
687 uniqueness of the interaction between the *SR3G* and *WRKY75* (**Fig. 9E**).

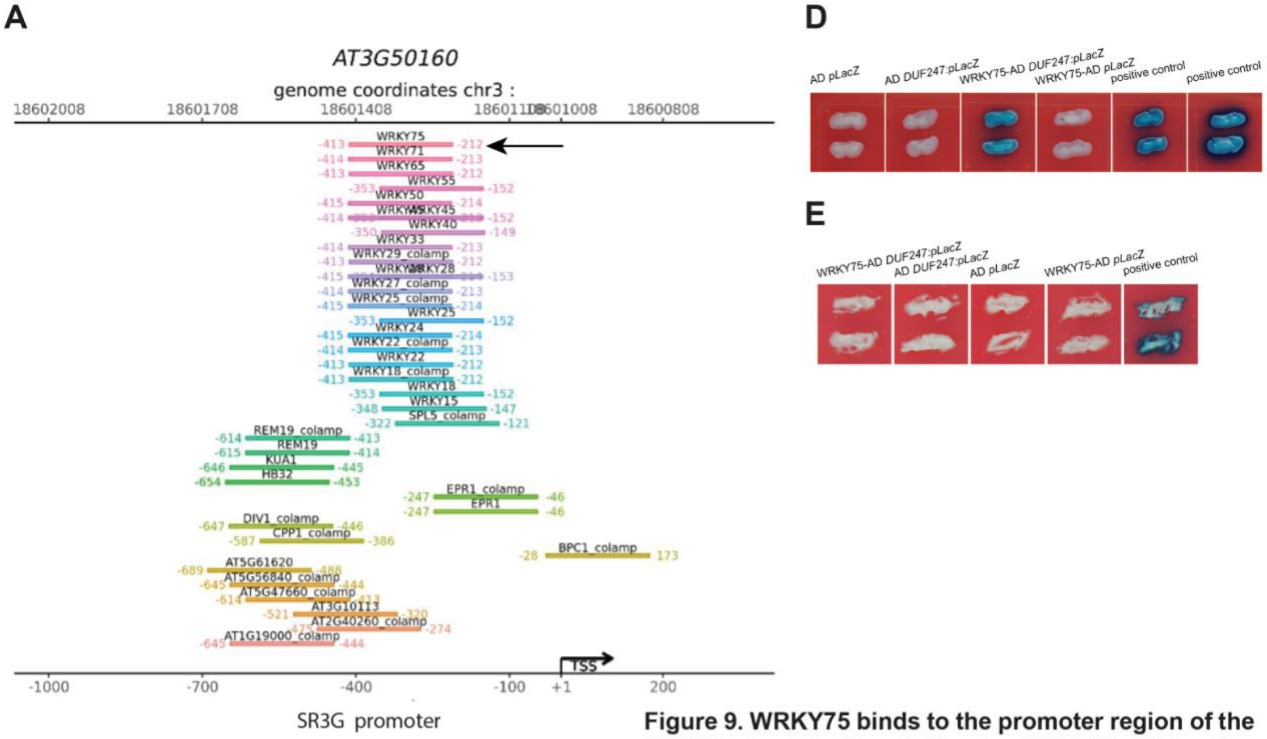

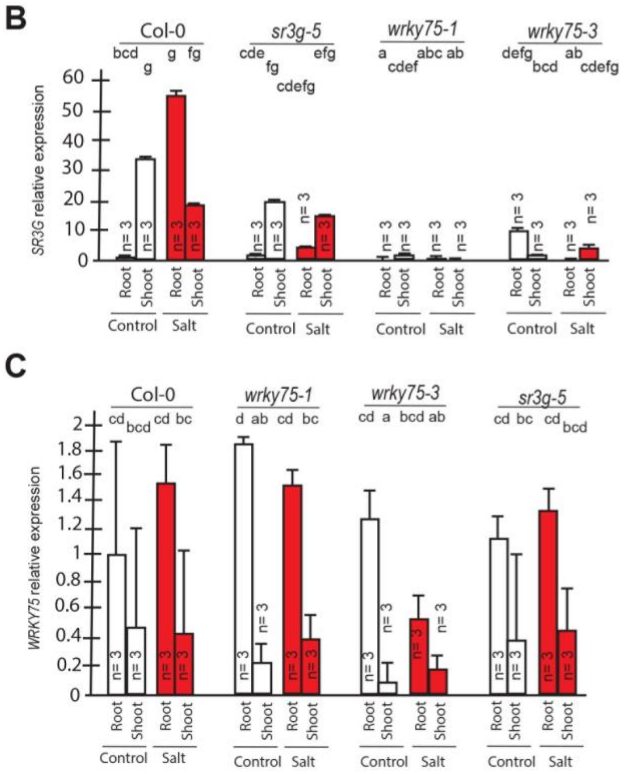

Figure 9. WRKY75 binds to the promoter region of the SR3G but not to its neighboring DUF247. (A) In silico searches in CisCross (https://plamorph.sysbio.ru/cis-cross/CCL_index.html) shows potential transcription factors with binding sites on the main SR3G (At3g50160) promoter region. A black-arrow points to the WRKY75 (AT5G13080). **(B)** RT-qPCR showing expression of SR3G (AT3G50160) and **(C)** WRKY75 (AT5G13080) genes, respectively, in Col-0, sr3g-5 mutant, and two different mutant alleles of the wrky75, i.e., wrky75-1 and wrky75-3. RT-qPCR analyses were conducted using seedlings grown on 1/2x MS for 4 d and then followed by transferring to the treatment plates with or without 75 mM NaCl for one week. Mean values are shown ± SE, with three biological replicates used in each condition and genotype. AT4G04120 (transposable_element_gene) was used as a reference gene for normalization. Significance was determined by the Tukey–Kramer HSD test in JMP. Levels not connected by same letter are significantly different. **(D)** Yeast one-hybrid (Y1H) assay showing WRKY75 (438 bp) binds to the promoter region of the main SR3G (AT3G50160, 953 bp) **(E)** but not to its neighboring promoter, i.e. DUF247-150 (At3g50150, 631 bp) . pB42AD (AD) and pLacZ were used as effector and reporter construct, respectively. Effector and reporter constructs were co-transformed into yeast strain EGY48. Transformants were selected and grown on SD/-Trp-Ura medium. The interactions were observed on SD/-Trp/-Ura + X-Gal medium. Empty vector expressing AD domain and pLacZ were used as negative control. The two positive controls are NIGT1.4-GolS2 and NIGT1.4-GAE1. The oligo sequences used for Y1H and luciferase assay were provided in Table S4.

688

To further examine the functional consequences of the relationship between SR3G and WRKY75, we generated *wrky75-3/sr3g-5* double mutants, and examined their root system architecture alongside the single mutants and Col-0. Under control conditions, both *sr3g-5* and *wrky75-3* mutants showed significant reduction in main root length compared to Col-0 and the two double mutants (**Fig. 10A**). Under 75 mM salt, only *wrky75-3* showed significant reduction in main root length compared to all other genotypes tested, confirming the previously described salt sensitivity for *wrky75* mutant under salt stress (Lu et al. 2023). We have not observed any differences in main root length under 125 mM salt across all genotypes tested (**Fig. 10A**). Regarding lateral root number (**Fig. 10B**) and length (**Fig. 10C**), we observed significant reduction in lateral root number and length for the two single mutants, *sr3g-5* and *wrky75-3*, compared to other genotypes only under control condition (**Fig. 10B-C**). We further investigated Na^+ and K^+ accumulations as well as Na^+/K^+ ratio in plate grown seedlings (**Fig. 10D, Fig. S24**). At 75 mM salt concentration, a subtle reduction in root Na^+/K^+ ratio was observed in the *wrky75* single mutant compared to the other genotypes tested. Conversely, shoot Na^+/K^+ ratio exhibited a slight decrease in the two double mutants compared to the other three genotypes at 75 mM salt concentration. At 125 mM salt concentration, root Na^+/K^+ ratio decreased in the two double mutants compared to Col-0 and the two single mutants. Similarly, the two double mutants maintained lower Na^+/K^+ ratios compared to Col-0 and the two single mutants in shoot at 125 mM salt concentration (**Fig. 10D**), indicating that the *SR3G* mutation indeed compensated for the increased Na^+ accumulation observed in the *wrky75* mutant under salt stress.

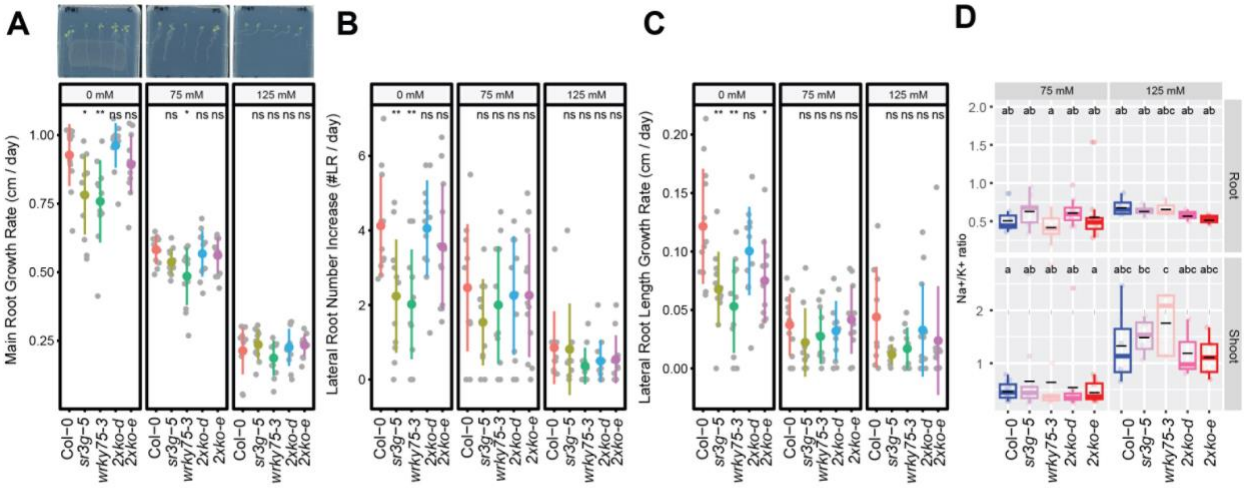

Figure 10. wrky75/sr3g double mutants roots exhibit reduced sensitivity to salt stress and accumulate lower levels of Na+ in their shoots. (A-C) Root system architecture analysis for the Col-0, sr3g-5, wrky75-3, and two double mutants under various concentrations of NaCl are shown here. Main root growth rate (A), Lateral root number increase (B), and Lateral root length increase (C) are shown for the indicated genotypes at various salt concentrations. **(D)** Na+/K+ ratio in root and shoot of indicated genotypes after two weeks on treatment plates. Each dot represents individual replicate per genotype. The asterisks above the graphs (A-C) indicate significant differences between Col-0 and the genotype, as determined by the Student 's t-test: *P < 0.05 and **P < 0.01. ns denotes no statistically significant. Statistical analysis in (D) was done by comparison of the means for all pairs using Tukey–Kramer HSD test. Levels not connected by the same letter are significantly different (P < 0.05).

Discussion

Exposure to abiotic stress alters plant architecture by affecting biomass distribution between individual organs (Julkowska and Testerink 2015; Guo et al. 2020). Exposure to drought alters the distribution of the biomass between root and shoot, to optimize water uptake, while limiting transpiration (Asch et al. 2005; Karcher et al. 2008; Uga et al. 2013; Chen et al. 2022). While the processes underlying salt-induced changes in shoot and root growth dynamics and architecture have been systematically described (Geng et al. 2013; Duan et al. 2013; Julkowska et al. 2017; Deolu-Ajayi et al. 2019; Yutao Zou et al. 2022; Awlia et al. 2021; Ariel et al. 2010), the methodological exploration of biomass distribution between root and shoot for plants exposed to salt stress is underexplored in the current body of research. Here, we developed a tool that allows a non-destructive quantification of root and shoot projected area of the seedlings grown on agar plates (**Fig. 1A**). This new tool allows us to efficiently describe changes in biomass accumulation and stress-induced alterations in root and shoot growth. Although the method is restricted to small plants and early developmental stages, it provides valuable insight into stress responses. The application of this tool to an Arabidopsis natural diversity panel revealed that salt stress exposure results in loss of coordination between root and shoot growth (**Fig. 1D**), rather than a clear directional change, as in the case of drought. To our knowledge, this is the first systematic study of changes in root:shoot ratio. The developed tool for quantifying root and shoot size in plate-grown Arabidopsis has the potential to significantly advance research by enabling developmental and stress studies, focusing on coordination of root and shoot development during seedling establishment. Facilitating detailed comparisons of root:shoot ratios, this tool can aid in formulating new hypotheses about the mechanisms contributing to seedling vigor and stress tolerance.

The natural variation in salt-induced changes in root:shoot ratio revealed a clear association with SNPs on chromosome 3 within *SR3G*, that is situated within a region containing eight other *DUF247* genes (**Fig. 2**). SR3G was previously associated with self-incompatibility in grasses (Lian et al. 2021; Crain et al. 2020), as well as with lesions and dwarfism in Arabidopsis (Kondou et al. 2013) through constitutive activation of defense responses. However, the *SR3G* associated with constitutive defense response was AT3G60470 (Kondou et al. 2013), which is located outside the interval associated with salt stress-induced changes in root:shoot ratio (**Fig. 2C**). Because we did not observe any consistent phenotypes in the T-DNA insertion lines of *DUF247s* neighboring the *SR3G* (**Fig. S19-20**), we examined the RNAi lines targeting multiple *DUF247s* including *SR3G* (**Fig. S21-23**). Our root system architecture analyses revealed no redundancy between *SR3G* and other DUF247s, and the reduced lateral root development in double mutants of RNAi lines simply mimics the phenotype of *sr3g-5* single mutant (**Fig. 6, Fig. S21**). Further, we demonstrated that only *SR3G* is regulated by *WRKY75* (**Fig. 9B-E**). As these genes are result of tandem duplication, they are expected to accumulate a lot of variation in the cis-regulatory regions. Therefore, differential regulation of two closely related genes can be expected by the accumulated variation within the promoter region.

The results acquired in this study provide multiple layers of evidence that support the role of *SR3G* as a negative regulator of salt stress response in Arabidopsis. Loss-of-function *SR3G* maintained higher shoot growth rate and larger rosette area when exposed to salt stress in the soil (**Fig. 7A-B**), probably due to reduced Na^+ accumulation (**Fig. 7D**), which in turn resulted in lower rates of cellular damage (**Fig. 7C**). This increased salt tolerance feature can be explained by the increased root suberization (**Fig. 7**) as suberin-deficient mutants show susceptibility to salt stress (Barberon et al. 2016; Ursache et al. 2021; Shukla et al. 2021). For example, Arabidopsis *CYP86A1/HORST* (At5g58860) encodes a cytochrome P450-dependent enzyme that is responsible for catalyzing fatty acid ω-hydroxylation. It plays a pivotal role in the biosynthesis of aliphatic suberin, particularly expressed in the root endodermis. Knock-out mutations of *CYP86A1/HORST* result in a substantial decrease of approximately 60% in total root suberin (Y. Li et al.

2007; Höfer et al. 2008). Consequently, the diminished aliphatic suberin content in the roots of *cyp86a1* mutants leads to increased permeability to water and solutes (Ranathunge and Schreiber 2011). Interestingly, *SR3G* expression is enhanced by salt stress (**Figs. 4, Fig. S13**), specifically in the root stele (**Fig. S13B**). The root stele encompasses vascular bundles, procambium and pericycle, which gives rise to the secondary growth and lateral root primordia respectively (Birnbaum et al. 2003). The stele is central to the systemic transport of water, minerals, and nutrients within the plant (B. Li et al. 2017; Ramachandran et al. 2020; Zarebanadkouki et al. 2019), and to the exclusion of salt ions from the transpiration stream (Møller et al. 2009).

The deposition of hydrophobic residues of lignin and suberin in the Casparian strips poses a significant barrier to apoplastic transport (Foster and Miklavcic 2017). Previously, silencing genes involved in Casparian strips formation resulted in increased lateral root development (X. Wang et al. 2020). As the suberization of the Casparian strips increases upon salt stress, it limits the accumulation of Na^+ and loss of K^+ ions from the root stele (Barberon et al. 2016). However, the effects of increased root suberization under salt stress have thus far not been described to affect lateral root development. Here, we have identified *SR3G* as a negative regulator of root suberization under salt stress (**Fig. 8**), which provides an additional layer of protection against sodium accumulation (**Fig. 8**), but negatively impacts lateral root development (**Fig. 6A-B**).

As SR3G was previously not described in the context of salt stress, we attempted to identify its molecular context through its transcriptional regulation. Through our *in-silico* analysis, we have identified *WRKY75* as a putative regulator of *SR3G* expression, and confirmed it using RT-qPCR and Y1H assay (**Fig. 9**). WRKY75 was previously described to act as a positive regulator of salt stress tolerance through activation of *SOS1* expression (Lu et al. 2023). Similar to previous study, we also observed *wrky75* mutants to be more sensitive to salt stress within our experiments (**Fig. 10A-C**). Nevertheless, when the *wrky75* mutation was coupled with *sr3g-5*, the roots displayed a phenotype identical to Col-0 (**Fig. 10A**), implying that the salt sensitivity of the *wrky75* mutant was counteracted by the *SR3G* mutation. Considering *WRKY75's* role in positively regulating *SOS1* expression during salt stress, it is plausible that its binding to the *SR3G* promoter inhibits its expression, thereby enhancing salt tolerance on a larger scale.

One of the main players in Na^+ transport is High-affinity K^+ Transporter (HKT1) (Laurie et al. 2002). HKT1 is expressed in root stele (Mäser et al. 2002), where it retrieves Na^+ from the transpiration stream and limits ion accumulation in the shoot, resulting in higher salt stress tolerance at later developmental stages (Møller et al. 2009). At early developmental stages, *HKT1* overexpression reduces the development of lateral root primordia (Julkowska et al. 2017), thus creating less Na^+ entry gate into the main root, resulting in less Na^+ accumulation in shoot. Similarly, *sr3g-5* mutants developed fewer lateral roots that are consistent with the lower Na^+ levels in the root upon salt stress (**Fig. 6**). The effects of HKT1 and SR3G differ in the magnitude of repression of lateral root development, with HKT1 mutants resulting in almost complete cessation of lateral root development (Julkowska et al. 2017), whereas repression of SR3G function has much more subtle phenotype. Whereas the effect of cell-type specific overexpression of HKT1 on plant performance was negative during the early developmental stage, due to impairing lateral root development, the *sr3g* mutants showed increased salt tolerance when exposed to salt stress treatment during their early vegetative growth (**Fig. 7**). These results suggest that reduced lateral root development under salt stress can have a gradient of responses leading to increased and decreased salt tolerance, and the effect is highly dependent on the wider physiological mechanisms, and their contributions to ion exclusion and maintained plant development throughout salt stress exposure.

In conclusion, the study of salt-induced changes in the root:shoot ratio, alongside the development of new tools to quantify these changes during the seedling establishment stage, represents an important new perspective into mechanisms underlying salt stress tolerance. Identification of SR3G as a novel regulator of root suberization, shoot growth, and Na^+ accumulation provides better understanding

of molecular mechanisms underlying plant responses to salt stress, but also offers a new avenue to explore more nuanced and tissue-specific strategies for enhancing salt stress tolerance.

Acknowledgments

The authors would like to thank BTI and KAUST Greenhouse Teams for their care of the plants. The authors would like to acknowledge support from the NSF-IOS #2023310 (ADLN) and NSF-IOS #2102120 (ADLN). The majority of funding for this work was generously provided from KAUST baseline funding awarded to Mark Tester, and BTI's startup funds awarded to Magdalena Julkowska.

Author contributions

M.M.J. and M.R.I. conceived the project and wrote the manuscript with inputs from all coauthors, C.T. and M.A.T. helped with conceiving the overall idea for the project, infrastructure and funding, R.A.H and R.S. developed the tool to quantify root and shoot size from Arabidopsis grown on agar plates, A.K. assisted with GWAS analysis, M.R.I. conducted majority of the experiments for functional characterization of *SR3G*, H.S., and M.D.A. performed molecular cloning of DR3G, H.S. screened other DUF247s T-DNA and RNAi mutant lines, L.J. performed the analysis of DUF247 domains that informed the cloning of individual SR3G fragments, G.D. and M.W. conducted GC-MS on suberin monomers, M.P. and E.C. performed ICP-AES, A.D.L.N. and L.Y. performed phylogenetic analysis, B.L. and Y.H. conducted Y1H.

Competing interests

The authors declare no competing interests.

Correspondence and requests for materials

To be addressed to Dr. Magdalena M. Julkowska (mmj55@cornell.edu)

Figure legends

Figure 1. Salt stress is causing discoordination of root and shoot growth. Arabidopsis HapMap population was screened for salt stress-induced changes in root:shoot ratio. The increase in the projected area of shoot and root (Fig. S2) was used to estimate growth rate of **(A)** shoot and **(B)** root using an exponential function. **(C)** The root:shoot growth rate ratio was calculated per genotype. The histograms represent the number of accessions acros three studied conditions (0, 75 and 125 mM NaCl), whereas the population average is indicated using the dashed line. Additionally, the distribution of the genotypes within each treatment was additionally visualized using the error plots (lower panel), where population average and standard error is indicated using a colored point and a line respectively. Individual grey points represent individual genotypes.

Figure 2. SR3G is associated with salt stress-induced changes in shoot-per-total seedling area ratio. The salt induced changes in root-to-shoot and shoot-per-total seedling area ratios were used as an input for GWAS. Manhattan plots representing the associations of shoot-per-total seedling area recorded 6 days after transfer to 125 mM NaCl and **(A)** 250 k SNPs and **(B)** 4 M SNPs. **(C)** Significant associations were found with the SNPs forming a locus on chromosome 3 in and around *SR3G* (AT3G50160), encoding Domain of Unknown Function 247 (DUF247). The natural variation in the LD region was studied in 162 accessions sequenced by 1001 Genomes Project. The upper panel represents portion of the missing data, upper middle panel represents deletions relative to Col-0, while lower middle panel represents the sequence similarity compared to Col-0. The bottom panel represents the open reading frames (ORFs) within the LD, and the location of associated SNPs is indicated with the dashed lines. Red dashed lines represent associations above Bonferroni threshold in 250k SNP mapping, while grey lines represent associations with -log10(p-value) > 5 in the 4M SNP mapping. **(D)** The haplotype analysis performed using SNPs located within the coding region of the SR3G revealed significant differences in shoot-per-total seedling area recorded 6 days after transfer to 125 mM NaCl between Haplotype groups 1 (represented by 46 accessions, including Col-0) and 11 (represented by 11 accessions, including Blh-1). The significant differences between individual haplotype groups were tested using ANOVA with Tukey HSD to identify significantly different groups. **(E)** Upon further sequencing of SR3G in accessions from Haplotype 1 and 11, revealed two 200 bp insertions within SR3G exons in 4 tested accessions belonging to haplotype 11 group. These 200 bp insertions resulted in a premature STOP-codon within the DUF247 domain (after Gly-215).

Figure 3. Phylogeny and positive selection analysis of *SR3G* and its orthologs from other species. The orthologous genes of *SR3G* (AT3G50160) from other seven species were identified using GoGeBlast (E-value < 1.00E-10). **(A)** The protein sequences of the 50 homologous genes were aligned by MUSCLE and then an unrooted phylogenetic tree was reconstructed by a Maximum -likelihood (ML)-derived style by RAxML (Bootstrap number: 100). **(B)** A positive selection analysis was conducted by branch-site model A test: Specifically, we hypothesized the differential or constant dN/dS (ω) substitution rate among the closely distant branches leading to DUF247 (AT3G50160) (See Method & Materials for details). These branches were marked as ω1 (light brown branch), ω2 (DUF247-specific branch), ω3 (light blue branch), and ω-rest (light purple branch). **(C)** The gene structure of DUF247 (AT3G50160) was illustrated by wide arrows (grey arrow: 5 and 3' UTR, yellow arrow: coding-region). The regions used for cloning (Fragment A, B, and C) were marked by narrow arrows along with "Coil-Coil Domain", "Putative Ca2+ binding fomain" and "Super-polar Fragment" marked on Fragment A and B, respectively. Lastly, the Bayes Empirical Bayes (BEB) was performed to test the probability of sites along with ω > 1 over the DUF247 (AT3G50160). Three sites were generated with a posterior probability > 0.90: 124C (P = 0.992), 206A (P = 0.951), and 209A (P

875 = 0.988). These three sites were marked with an orange asterisk and assumed to have been undergoing
876 positive selection.

877 **Figure 4. Transcript abundances for the two closely related *DUF247s.*** Expression of **(A)** *SR3G*
878 (AT3G50160) **(B)** and its closest homologue *DUF247-150* (AT3G50150) were measured in Col-0 seedlings
879 grown with and without salt stress. RT-qPCR analyses were conducted using seedlings grown on 1/2x MS
880 for 4 d and then followed by transferring to the treatment plates with or without 75 mM NaCl for one
881 week. Mean values are shown ± SE, with number of replicates (n) shown in each graph. *AT4G04120* was
882 used as a reference gene for normalization. Significance was determined by the Tukey–Kramer HSD test
883 in JMP.

884 **Figure 5. SR3G full-length protein resides in the plasma membrane while removal of its transmembrane**
885 **domain results in protein relocation to nucleus and cytosol.** SR3G full-length protein **(A-B)** or truncated
886 versions **(C-E)** fused to mVenus at the N-terminus were agro-infiltrated into the *Nicotiana benthamiana*
887 leaves for transient expression. Shown are a bright-field image of transfected leaf cells and mVenus-SR3G-
888 mediated fluorescence as well as GFP-based subcellular marker. **(A)** Localization of full-length SR3G alone
889 or **(B)** in combination with the known plasma membrane dye, FM4-64. Localization of truncated versions
890 of SR3G are shown for **(C)** SR3G-Fragment A, **(D)** SR3G-Fragment B, and **(E)** SR3G-Fragment AB. **(F)** Free
891 GFP was used as a nuclear and cytosolic marker. Scale bar = 25 µm.

892 **Figure 6. *sr3g* mutant displays reduced growth rate for the lateral root length and Na^+ content in the**
893 **root.** Root system architecture analysis of Col-0 and *sr3g-5* genotypes under various concentrations of
894 NaCl are shown here. **(A)** Shown are representative images of 13-day-old Col-0 and *sr3g-5* genotypes that
895 experienced 9 days of salt treatment at indicated concentrations as well as growth rate for lateral root
896 length. **(B)** Salt Tolerance Index (STI) for the main root length, average lateral root length, and lateral root
897 number at 75 mM NaCl. The STI was calculated by dividing the growth rate measured under salt stress by
898 the growth rate measured under control condition for each genotype. **(C)** Na^+/K^+ ratio in root and shoot
899 of Col-0 and *sr3g-5* after two weeks on 75 mM salt are shown. Each dot in (A) and (B) represents individual
900 replicate per genotype. Lines in (A) and (B) graphs represent median and average, respectively. In (A) and
901 (B), the asterisks above the graphs indicate significant differences between Col-0 and the *sr3g-5* mutant,
902 as determined by the Student 's t-test: $*P < 0.05$. Statistical analysis in (C) was done by comparison of the
903 means for all pairs using Tukey–Kramer HSD test. Levels not connected by the same letter are significantly
904 different ($P < 0.05$). Root system architecture and ICP-AES analyses of Col-0 and *sr3g-5* mutant are shown
905 in details in **Figure S17**.

906 **Figure 7. *sr3g* mutant has higher growth rate and larger rosette area while displaying less ion leakage**
907 **and Na^+ accumulation in shoot under salt stress.** The salt stress responses of 2-week-old (referred to as
908 "early salt stress") or 3-week-old (referred to as "late salt stress") soil-grown Col-0 and *sr3g-5* plants that
909 were exposed to a final concentration of 100 mM NaCl were examined here. **(A)** Rosette growth rate and
910 **(B)** area were monitored over a period of two weeks, during which the "early salt stress" group
911 experienced two weeks of salt stress while the "late salt stress" group experienced one week.
912 Representative images of 4-week-old Col-0 and *sr3g-5* genotypes were shown in (A). **(C)** Ion leakage
913 percentage, **(D)** Na^+ and **(E)** K^+ contents in shoot were measured in 4-week-old plants. Each line in (A) and
914 (B) represents the trajectory per genotype through time, where red and blue lines indicate Col-0 and *sr3g-*
915 *5* plants grown under control or salt-stress conditions, respectively. The dashed lines represent the mean
916 values of the genotype per condition, whereas the grey band represents the confidence interval. The
917 asterisks above the graphs indicate significant differences between Col-0 and *sr3g-5* plants, as determined
918 by one-way analysis of variance: $*P < 0.05$, $**P < 0.01$, $***P < 0.001$, and $****P < 0.0001$. Statistical

919 analysis in (C) to (E) was done by comparison of the means for all pairs using Tukey–Kramer HSD test.
920 Levels not connected by the same letter are significantly different ($P < 0.05$).

921 **Figure 8. *sr3g* mutant root is more suberized than Col-0. (A)** Representative images of fluorol yellow (FY)
922 staining of four root sections (# 1 to 4, from root tip to root base as shown by white rectangles across the
923 seedling) were shown for Col-0 and *sr3g-5* mutant with or without 75 mM NaCl. Seeds were germinated
924 on the 1/2 MS plates for 4 d and then seedlings were transferred to the treatment plates with or without
925 75 mM NaCl for 2 more days. **(B)** Quantification of FY signal intensity for each root section. The FY
926 quantification was done using ImageJ. Scale bar is equal to 500 µm in all. **(C)** Suberin monomers detected
927 using Gas Chromatography–Mass Spectrometry (GC-MS) in the Col-0 and *sr3g-5* mutant roots with or
928 without 75 mM NaCl included fatty acid (FA), fatty alcohol (OH-FA), α,ω-dicarboxylic acids (DCA), and ω-
929 hydroxy fatty acid (ωOH-FA). The significant differences between Col-0 and *sr3g-5* mutant were evaluated
930 using Student 's t-test.

931 **Figure 9. WRKY75 binds to the promoter region of the *SR3G* but not to its neighboring DUF247. (A)** In
932 silico searches in CisCross (https://plamorph.sysbio.ru/ciscross/CCL_index.html) shows potential
933 transcription factors with binding sites on the main *SR3G* (At3g50160) promoter region. A black-arrow
934 points to the *WRKY75* (AT5G13080). RT-qPCR showing expression of *SR3G* (AT3G50160) **(B)** and *WRKY75*
935 (AT5G13080) **(C)** genes, respectively, in Col-0, *sr3g-5* mutant, and two different mutant alleles of the
936 *wrky75, i.e., wrky75-1* and *wrky75-3*. RT-qPCR analyses were conducted using seedlings grown on 1/2x
937 MS for 4 d and then followed by transferring to the treatment plates with or without 75 mM NaCl for one
938 week. Mean values are shown ± SE, with three biological replicates used in each condition and genotype.
939 *AT4G04120* (transposable_element_gene) was used as a reference gene for normalization. Significance
940 was determined by the Tukey–Kramer HSD test in JMP. Levels not connected by same letter are
941 significantly different. Yeast one-hybrid (Y1H) assay showing *WRKY75* (438 bp) binds to the promoter
942 region of the main *SR3G* (AT3G50160, 953 bp) **(D)** but not to its neighboring promoter, i.e. DUF247-150
943 (At3g50150, 631 bp) **(E)**. *pB42AD* (AD) and *pLacZ* were used as effector and reporter construct,
944 respectively. Effector and reporter constructs were co-transformed into yeast strain EGY48.
945 Transformants were selected and grown on SD/-Trp-Ura medium. The interactions were observed on SD/-
946 Trp/-Ura + X-Gal medium. Empty vector expressing AD domain and *pLacZ* were used as negative control.
947 The two positive controls are NIGT1.4-GolS2 and NIGT1.4-GAE1. The oligo sequences used for Y1H and
948 luciferase assay were provided in **Table S4.**

949 **Figure 10. *wrky75/sr3g* double mutants roots exhibit reduced sensitivity to salt stress and accumulate**
950 **lower levels of Na^+ in their shoots. (A-C)** Root system architecture analysis for the Col-0, *sr3g-5, wrky75-*
951 *3,* and two double mutants under various concentrations of NaCl are shown here. Main root growth rate
952 **(A)**, Lateral root number increase **(B)**, and Lateral root length increase **(C)** are shown for the indicated
953 genotypes at various salt concentrations. **(D)** Na^+/K^+ ratio in root and shoot of indicated genotypes after
954 two weeks on treatment plates. Each dot represents individual replicate per genotype. The asterisks
955 above the graphs (A-C) indicate significant differences between Col-0 and the genotype, as determined
956 by the Student 's t-test: $*P < 0.05$ and $**P < 0.01$. ns denotes no statistically significant. Statistical analysis
957 in (D) was done by comparison of the means for all pairs using Tukey–Kramer HSD test. Levels not
958 connected by the same letter are significantly different ($P < 0.05$).
959

Supplemental figure and table legends

Figure S1. Evaluation of the tool's precision for estimating seedling size. The tool used to quantify root and shoot size from the agar plates was tested on the Arabidopsis Col-0 seedlings exposed to various concentrations of salt stress (0, 75 and 125 mM NaCl). The fresh weight of root and shoot of individual plants were recorded at the last day of experiment (8 days after transfer to treatment plates, 12 days after germination), and the correlation analysis between individual organ's fresh weight and area was performed in R. The Correlation co-efficient and the p-value for individual correlations were calculated in R using stats package.

Figure S2. Salt stress reduced the increase in root and shoot area over time across HapMap accession. Four-days-old seedlings exposed to 0, 75 and 125 mM NaCl grown on agar plates were scanned every 2nd day and analyzed for root and shoot area using a custom tool. The change in genotype-specific **(A)** shoot and **(B)** root area was calculated in R using stats package. The thick dashed lines represent population-wide average in root and shoot area over the time of the experiment, while individual transparent lines indicate change in root and shoot area for individual accession. The differences between control and individual salt stress treatments were evaluated using ANOVA. The *, **, *** and **** represent p-values below 0.05, 0.01, 0.001 and 0.0001 respectively.

Figure S3. Salt stress induced changes in relative growth of shoot, root and root:shoot ratio. The stress tolerance index was calculated for shoot, root and root:shoot ratio by dividing genotype specific value recorded at salt stress over the genotypic mean of the trait recorded under non-stress conditions. Individual points represent individual genotypes. The population mean for 75 and 125 mM NaCl treated plants is represented by the colored point, whereas the population-wide standard error.

Figure S4. The correlation between all measured traits and calculated stress tolerance indices (STI). The correlations between all measured and calculated traits was performed using the Pearson's correlation coefficient. All non-significant correlations were replaced by blank circles. The size and color of individual circles indicates the strength and significance of individual correlation between two traits. Blue and red shades indicate positive and negative correlations respectively.

Figure S5. The correlation between total seedling area and salt-induced changes in the root-to-shoot ratio. The correlation between the total seedling area quantified using the custom tool at the last day of experiment (8 days after transfer and 12 days after germination), and the ratio of root-and-shoot growth rate was examined across Arabidopsis HapMap population and various concentrations of salt stress (0, 75 and 125 mM NaCl). The correlation analysis was performed in R, and the Correlation co-efficient (r) and the p-values for individual correlations were calculated in R using stats package.

Figure S6. Region around NTL8 is associated with salt stress-induced changes in root-per-shoot growth. The salt induced changes in root-to-shoot and shoot-per-total seedling area ratios were used as an input for GWAS. **(A)** Manhattan plot represents the associations of root-per-shoot growth factors recorded at 75 mM NaCl with 250 k SNPs while **(B)** represents the QQ plot for this association study. **(C)** Significant associations were found with the SNPs forming a locus on chromosome 2 in and around AT2G27300, encoding a NAC-domain containing transcription factor (NTL8). The natural variation in the LD region was studied in 162 accessions sequenced by 1001 Genomes Project. The upper panel represents portion of the missing data, upper middle panel represents deletions relative to Col-0, while lower middle panel represents the sequence similarity compared to Col-0. The bottom panel represents the open reading frames (ORFs) within the LD, and the location of associated SNPs is indicated with the dashed lines. Red

1002 dashed lines represent associations above Bonferroni threshold in 250k SNP mapping, while grey lines
1003 represent associations with -log10(p-value) > 5 in the 4M SNP mapping.

1004 **Figure S7. Region around unknown gene is associated with salt stress-induced changes in relative**
1005 **changes in shoot-per-total seedling area.** The salt induced changes in root-to-shoot and shoot-per-total
1006 seedling area ratios were used as an input for GWAS. **(A)** Manhattan plot represents the associations of
1007 relative change (125 mM / 0 mM) in shoot-per-total seedling area at 4 days after transfer to 125 mM NaCl,
1008 while **(B)** represents the QQ plot for this association study. **(C)** Significant associations were found with
1009 the SNPs forming a locus on chromosome 3 in and around AT3G22430, encoding an unknown gene
1010 encoding a domain of unknown function. The natural variation in the LD region was studied in 162
1011 accessions sequenced by 1001 Genomes Project. The upper panel represents portion of the missing data,
1012 upper middle panel represents deletions relative to Col-0, while lower middle panel represents the
1013 sequence similarity compared to Col-0. The bottom panel represents the open reading frames (ORFs)
1014 within the LD, and the location of associated SNPs is indicated with the dashed lines. Red dashed lines
1015 represent associations above Bonferroni threshold in 250k SNP mapping, while grey lines represent
1016 associations with -log10(p-value) > 5 in the 4M SNP mapping.

1017 **Figure S8. The QQ-plots for GWAS models with shoot-per-total seedling area.** The QQ-plots for
1018 association between shoot-per-total seedling area recorded 6 days after transfer to 125 mM NaCl and **(A)**
1019 250 k SNPs and **(B)** 4 M SNPs. The red line indicates the expected vs. observed ratio of association, while
1020 black points indicate the observed associations.

1021 **Figure S9. Haplotype analysis of AT3G50160 (SR3G).** The haplotype analysis performed using SNPs
1022 located within the coding region of the SR3G (AT3G50160) revealed significant differences in **(A)** Relative
1023 shoot growth (as fraction of shoot growth at 125 mM NaCl and 0 mM NaCl) and **(B)** Shoot growth at 125
1024 mM NaCl. The significant differences between individual haplotype groups (each haplotype represented
1025 by at least 3 accessions), were tested using ANOVA with Tukey HSD to identify significantly different
1026 groups. Significant differences were identified between Haplotype groups 1 (represented by 46
1027 accessions, including Col-0) and 11 (represented by 11 accessions, including Blh-1).

1028 **Figure S10. Nucleotide sequence alignment of SR3G CDS between Col-0 and Blh-1 alleles.** The nucleotide
1029 sequences from SR3G CDS were obtained from Col-0 and Blh-1 cDNA, and compared to Col-0 cDNA
1030 sequence on TAIR. The cDNA sequences were subsequently aligned in JalView using ProbconsWS
1031 alignment. The intensity of purple hue indicates the nucleotide identity, while dash marks indicate
1032 insertion in Blh-1 compared to Col-0 allele.

1033 **Figure S11. Amino acid sequence alignment of SR3G CDS between Col-0 and Blh-1 alleles.** The amino
1034 acid sequences from SR3G CDS were obtained by translating Col-0 and Blh-1 cDNA into amino acid
1035 sequence in JalView using Standard settings. The amino acid sequences were subsequently aligned in
1036 JalView using ProbconsWS alignment. The sequence length markers for are indicated above the aligned
1037 sequence. The intensity of purple hue is indicating the nucleotide identity, while dash marks indicate
1038 insertion in one of the alleles. * indicate STOP codons.

1039 **Figure S12. Sequence alignment between Col-0 and Blh-1 alleles for SR3G promotor.** The nucleotide
1040 sequences from SR3G promotor were obtained from Col-0 and Blh-1 genomic DNA, and compared to Col-
1041 0 sequence on TAIR. The gDNA sequences were subsequently aligned in JalView using ProbconsWS
1042 alignment. The intensity of purple hue is indicating the nucleotide identity, while dash marks indicate
1043 insertions.

1044 **Figure S13. Gene expression profile of *SR3G* across various developmental stages and salt stress.** The
1045 absolute gene expression of *SR3G* is depicted across various developmental stages **(A)**, root cell types **(B)**,
1046 and in response to salt-induced changes **(C)**. The images were acquired through the eFP Browser using
1047 data sources specified for the developmental map, abiotic stress, and tissue specific.

1048 **Figure S14. Gene expression profile of other *DUF247s* under salt stress.** Absolute gene expression of
1049 other *DUF247s* are depicted in response to salt-induced changes. The images were acquired through the
1050 eFP Browser using data sources specified for the abiotic stress. The *SR3G* is shown in a green box for
1051 comparison.

1052 **Figure S15. SR3G predicted protein domains.** The SR3G protein sequence (Col-0 allele) was used to
1053 identify predicted protein domains. The identified domains include: nuclear localization signal (NLS): K15-
1054 F19; coiled-coil domain: M153-K173; potential Ca2+ binding pocket: G210-F372; and transmembrane
1055 domain P469-T503. Informed by these predicted protein domains, we designed SR3G Fragment A, B and
1056 C for subsequent localization studies and functional characterization. The pink mark at Y216 indicates a
1057 position of a premature STOP codon in Blh-1 allele.

1058 **Figure S16. The expression of *DUF247-150* remains unaltered in the *sr3g* mutant. (A)** Schematic diagram
1059 of main *SR3G* gene model and the location of T-DNA insertions. The location of T-DNA insertions is shown
1060 for *sr3g-4*, and *-5* mutants using triangles. RT-qPCR showing expression of *SR3G* gene (AT3G50160) **(B)**
1061 and its neighboring gene, *DUF247-150* (At3g50150) **(C)** in Col-0 and two *sr3g* mutants. RT-qPCR analyses
1062 were conducted using seedlings grown on 1/2x MS for 4 d and then followed by transferring to the
1063 treatment plates with or without 75 mM NaCl for one week. Mean values are shown ± SE, with the number
1064 of replicates (n) shown in each graph. *AT4G04120* (transposable_element_gene) was used as reference
1065 gene for normalization. Significance was determined by the Tukey–Kramer HSD test in JMP. Levels not
1066 connected by same letter are significantly different.

1067 **Figure S17. *sr3g-5* mutant displays no difference in main root length and lateral root numbers compared**
1068 **to Col-0.** Root system architecture analysis of Col-0 and *sr3g-5* genotypes under various concentrations
1069 of NaCl are shown here for main root length **(A)** and increase in lateral root number **(B)**. 13-day-old Col-0
1070 and *sr3g-5* genotypes experienced 9 days of salt treatment at indicated concentrations were used here.
1071 Each dot in (A) and (B) represents individual replicate per genotype. Statistical analysis was performed
1072 between Col-0 and the *sr3g-5* mutant using the Student 's t-test: $*P < 0.05$. **(C)** Na^+, **(D)** K^+ contents as well
1073 as Na^+/K^+ ratio **(E)** in root and shoot of Col-0 and *sr3g-5* after two weeks on 75 mM salt are shown.
1074 Statistical analysis in **(C-E)** was done by comparison of the means for all pairs using Tukey–Kramer HSD
1075 test. Levels not connected by the same letter are significantly different ($P < 0.05$).

1076 **Figure S18. *sr3g-4* mutant has no alteration in root system architectures compared to Col-0.** Root system
1077 architecture analysis of Col-0 and *sr3g-4* genotypes under various concentrations of NaCl are shown here
1078 for main root length **(A)**, lateral root length **(B)**, and lateral root number **(C)**. Salt Tolerance Index (STI) for
1079 the main root length, average lateral root length, and lateral root number are shown at 75 **(D)** and 125 **(E)**
1080 mM NaCl, respectively. The STI was calculated by dividing the growth rate measured under salt stress by
1081 the growth rate measured under control condition for each genotype. Statistical analysis was performed
1082 between Col-0 and the *sr3g-4* mutant using the Student 's t-test: $*P < 0.05$.

1083 **Figure S19. Root system architecture analysis of neighboring DUF247 mutants under the salt.** Main root
1084 length **(A)**, lateral root number **(B)**, and lateral root length **(C)** are shown for neighboring *DUF247s* of the
1085 *SR3G*, including At3g50120 (shown as 120, with one T-DNA representative, 120-2(SAIL_382_A09)),

At3g50140 (shown as 140, with three T-DNA representatives, 140-1 (SALK_044685), 140-2 (SALK_005466), and 140-3 (SALK_122700)), At3g50150 (shown as 150, with two T-DNA representatives, 150-1 (SALK_003824) and 150-3 (SALK_071080)), and At3g50170 (shown as 170, with two T-DNA representatives, 170-1 (SALK_009186) and 170-2 (SALK_112602)) compared to Col-0 under various concentrations of NaCl as indicated. The corresponding Salt Tolerance Index (STI) was calculated for main root growth **(D)**, increase in lateral root number **(E)**, and lateral root length **(F)**. Statistical analysis was performed between Col-0 and the other mutants using the Student 's t-test: $*P < 0.05$. The root system architecture analysis was performed similar to what described for Figure 6.

Figure S20. Root system architecture analysis of neighboring DUF247 mutants under the salt, continues. Main root length **(A)**, lateral root number **(B)**, and lateral root length **(C)** are shown for neighboring of the *SR3G*, including At3g50170 (shown as 170, with three T-DNA representatives, 170-3F (SALK_008710), 170-4F (SALK_145999), 170-5A (SALK_072937)), At3g50190 (shown as 190, with one T-DNA representative, 190-2B (SALK_137791)), and At3g50200 (shown as 200, with three T-DNA representatives, 200-1A (SALK_113759), 200-2B (SALK_093701), and 200-3B (SALK_129634)) compared to Col-0 under various concentrations of NaCl as indicated. The corresponding Salt Tolerance Index was calculated for main root growth **(D)**, increase in lateral root number **(E)**, and lateral root length **(F)**. Statistical analysis was performed between Col-0 and the other mutants using the Student 's t-test: $*P < 0.05$. The root system architecture analysis was performed similar to what described for Figure 6.

Figure S21. Root system architecture analysis of RNAi lines targeting neighboring DUF247s. Main root length **(A)**, main root length tolerance index **(B)**, lateral root length **(C)**, lateral root length tolerance index **(D)**, lateral root number **(E)**, and lateral root number tolerance index **(F)** are shown for RNAi lines targeting AT3G50140 (CSHL3-F1a), targeting AT3G50130 and AT3G50140 (CSHL6-C2d), targeting AT3G50150 and AT3G50170 (CSHL11-F1b), targeting AT3G50140 and AT3G50170 (CSHL13-F2a), targetingAT3G50150 and AT3G50190 (CSHL18-K4c), targeting AT3G50130, AT3G50140, AT3G50150, AT3G50160, AT3G50170, AT3G50180, and AT3G50190 (CSHL19-E2c), targeting AT3G50130 and AT3G50150 (CSHL21-E2a), and targeting AT3G50150 and AT3G50160 (CSHL22-F1c). Statistical analysis was performed between Col-0 and the RNAi lines using a Student's t-test: $*P < 0.05$, $**P < 0.01$, $***P < 0.001$, $****P < 0.0001$.

Figure S22. Root system architecture analysis of RNAi lines targeting neighboring DUF247s continued. Main root length **(A)**, main root length tolerance index **(B)**, lateral root length **(C)**, lateral root length tolerance index **(D)**, lateral root number **(E)**, and lateral root number tolerance index **(F)** are shown for RNAi lines targeting AT3G50160 (CSHL4-B2a and CSHL4G1d), targeting AT3G50140 and AT3G50150 (CSHL7-A3a), targeting AT3G50140 and AT3G50190 (CSHL8-G2b), targeting AT3G50180 (CSHL10-I1c), targeting AT3G50130, AT3G50140, AT3G50170, AT3G50180, and AT3G50190 (CSHL12-A1a), targeting AT3G50140, AT3G50170, AT3G50180, and AT3G50190 (CSHL15-E1b), targeting AT3G50130, AT3G50160, and AT3G50170 (CSHL-A2c and CSHL16-B1a), targeting AT3G50130 and AT3G50160 (CSHL20-G3b), and targeting AT3G50130 and AT3G50150 (CSHL21-L2c and CSHL21-M1d). Statistical analysis was performed between Col-0 and the RNAi lines using a Student's t-test: $*P < 0.05$, $**P < 0.01$, $***P < 0.001$, $****P < 0.0001$.

Figure S23. Root system architecture analysis of RNAi lines targeting neighboring DUF247s continued. Main root length **(A)**, main root length tolerance index **(B)**, lateral root length **(C)**, lateral root length tolerance index **(D)**, lateral root number **(E)**, and lateral root number tolerance index **(F)** are shown for RNAi lines targeting AT3G50140 (CSHL3-F3a), targeting AT3G50160 (CSHL4-D1c3, CSHL4-D4a, and CSHL4-F1b), targeting AT3G50130 and AT3G50170 (CSHL5-D3b and CSHL5-E2b), targeting AT3G50130 and AT3G50140 (CSHL6-B1c), targeting AT3G50140 and AT3G50150 (CSHL7-C1b2), targeting AT3G50140 and

1130 AT3G50190 (CSHL8-D3b and CSHL8-H1d), targeting AT3G50180 (CSHL10-I1b), targeting AT3G50150 and
1131 AT3G50170 (CSHL11-E5b), targeting AT3G50130, AT3G50140, AT3G50170, AT3G50180, and AT3G50190
1132 (CSHL12-B1a and CSHL12-D1c), targeting AT3G50140 and AT3G50170 (CSHL13-F1b and CSHL13-F4d),
1133 targeting AT3G50140, AT3G50170, AT3G50180, and AT3G50190 (CSHL15-G1a1 and CSHL15-H2b),
1134 targeting AT3G50150 and AT3G50190 (CSHL18-E4c and CSHL18-I2d), targeting AT3G50130, AT3G50140,
1135 AT3G50150, AT3G50160, AT3G50170, AT3G50180, and AT3G50190 (CSHL19-F1a, CSHL19-I3c, and
1136 CSHL19-L1c), and targeting AT3G50130 and AT3G50160 (CSHL20-F2b). Statistical analysis was performed
1137 between Col-0 and the RNAi lines using a Student's t-test: $*P < 0.05$, $**P < 0.01$, $***P < 0.001$, $****P <$
1138 0.0001.

1139 **Figure S24. *wrky75/sr3g* double mutants exhibit higher shoot K^+ contents compared to Col-0 and each**
1140 **individual single mutant in the presence of 125 mM salt. (A)** Na^+ and **(B)** K^+ contents in root and shoot
1141 of Col-0, *sr3g-5, wrky75-3,* and two double mutants under various concentrations of NaCl are shown here.
1142 Statistical analysis in (A-B) was done by comparison of the means for all pairs using Tukey–Kramer HSD
1143 test. Levels not connected by the same letter are significantly different ($P < 0.05$).

1144 **Figure S25. *wrky75/sr3g* double mutants exhibit no noticeable differences in rosette area compared to**
1145 **their individual single mutants when grown in saline soil.** The salt stress responses of 2-week-old soil-
1146 grown plants that were exposed to a final concentration of 100 mM NaCl were examined here. Rosette
1147 area **(A)** and growth rate for each individual day were shown **(B-M)**. Growth rate is shown for 1 **(B)**, 2 **(C)**,
1148 and 3 **(D)** days before the stress, respectively. Growth rate is shown for 1 **(E)**, 2 **(F)**, 3 **(G)**, 4 **(H)**, 5 **(I)**, 6 **(J)**,
1149 7 **(K)**, 8 **(L)**, and 9 **(M)** days of stress application, respectively. Na+/K+ **(N)** ratio in shoot were measured in
1150 4-week-old plants. Each line in (A) represents the trajectory per genotype through time. The effect of the
1151 genotype within individual treatment in (B-M) was tested using ANOVA, and the significantly different
1152 genotypes were additionally determined using Tukey HSD test (pvalue < 0.05). Statistical analysis in (N)
1153 was done by comparison of the means for all pairs using Tukey–Kramer HSD test. Levels not connected by
1154 the same letter are significantly different ($P < 0.05$).

1155 **Table S1. The individual traits recorded and calculated from the HapMap accessions exposed to the**
1156 **three different levels of salt stress.** The root and shoot projected area were quantified using a custom
1157 developed tool. The change in the root and shoot area over time was used to calculate Growth Factor (GF)
1158 by fitting an exponential function. The broad sense heritability (H2) was calculated for each trait over
1159 individual days and conditions using MVApp.

1160 **Table S2. Genotypic mean data used as an input for GWAS.** The genotypic mean data was calculated
1161 from at least 4 biological replicates per genotype per condition. The root and shoot area were extracted
1162 using a custom developed tool. The Growth Factors (GF) for root and shoot were calculated using
1163 exponential growth function. Total seedling slze (Tot) was calculated by adding root and shoot area for
1164 individual day. Shoot per Total (SpT) ratio was calculated for individual days by dividing genotype specific
1165 shoot area by the total seedling area for that day and condition. Root per Shoot ratio (RpS) was calculated
1166 by dividing genotype specific root area by the shoot area for that day and condition.

1167 **Table S3. Significant associations identified with GWAS of all used traits.** The location of individual SNPs
1168 is listed according to its location on Chromosome (Chr) and position (Pos). The individual SNP Minor Allele
1169 Count (MAC) and Minor Allele Frequency (MAF) is calculated based on specific SNP set used (4 Million or
1170 250 Thousand – listed in "Mapping" column). The traits associated with individual SNPs are abbreviated
1171 as RpS for Root-per-Shoot, SpT for Shoot-per-Total seedling area, Tot for Total seedling area, GR for
1172 growth rate and SHIIT for Shoot Ion Independent Tolerance index (Salt / Control).

1173 **Table S4. Most important GWAS associations.** The most important associations identified through GWAS
1174 (Table S3) were inspected further for their functions using either T-DNA or RNAi mutant lines. List of
1175 oligoes used for genotyping, RT-qPCR, cloning, and Y1H assay are provided.

1176 **Table S5. The gene ID, species, and gene names used for identification of SR3G orthologs and**
1177 **paralogs.**

1178 **Table S6. Links to cloning construct maps generated in this study.**
1179

References

1001 Genomes Consortium. Electronic address: magnus.nordborg@gmi.oeaw.ac.at, and 1001 Genomes Consortium. 2016. "1,135 Genomes Reveal the Global Pattern of Polymorphism in Arabidopsis Thaliana." *Cell* 166 (2): 481–91.

Abrol, I. P., Jai Singh Pal Yadav, and F. I. Massoud. 1988. *Salt-Affected Soils and Their Management*. Food & Agriculture Org.

Ariel, Federico D., Anouck Diet, Martin Crespi, and Raquel L. Chan. 2010. "The LOB-like Transcription Factor MtLBD1 Controls Medicago Truncatula Root Architecture under Salt Stress." *Plant Signaling & Behavior* 5 (12): 1666–68.

Asch, Folkard, Michael Dingkuhn, Abdoulaye Sow, and Alain Audebert. 2005. "Drought-Induced Changes in Rooting Patterns and Assimilate Partitioning between Root and Shoot in Upland Rice." *Field Crops Research* 93 (2): 223–36.

Awlia, Mariam, Nouf Alshareef, Noha Saber, Arthur Korte, Helena Oakey, Klára Panzarová, Martin Trtílek, Sónia Negrão, Mark Tester, and Magdalena M. Julkowska. 2021. "Genetic Mapping of the Early Responses to Salt Stress in Arabidopsis Thaliana." *The Plant Journal: For Cell and Molecular Biology* 107 (2): 544–63.

Awlia, Mariam, Arianna Nigro, Jiří Fajkus, Sandra M. Schmoeckel, Sónia Negrão, Diana Santelia, Martin Trtílek, Mark Tester, Magdalena M. Julkowska, and Klára Panzarová. 2016. "High-Throughput Non-Destructive Phenotyping of Traits That Contribute to Salinity Tolerance in Arabidopsis Thaliana." *Frontiers in Plant Science* 7 (September): 1414.

Bacher, Harel, Yoav Sharaby, Harkamal Walia, and Zvi Peleg. 2022. "Modifying Root-to-Shoot Ratio Improves Root Water Influxes in Wheat under Drought Stress." *Journal of Experimental Botany* 73 (5): 1643–54.

Barberon, Marie, Joop Engelbertus Martinus Vermeer, Damien De Bellis, Peng Wang, Sadaf Naseer, Tonni Grube Andersen, Bruno Martin Humbel, et al. 2016. "Adaptation of Root Function by Nutrient-Induced Plasticity of Endodermal Differentiation." *Cell* 164 (3): 447–59.

Baxter, Ivan, Prashant S. Hosmani, Ana Rus, Brett Lahner, Justin O. Borevitz, Balasubramaniam Muthukumar, Michael V. Mickelbart, Lukas Schreiber, Rochus B. Franke, and David E. Salt. 2009. "Root Suberin Forms an Extracellular Barrier That Affects Water Relations and Mineral Nutrition in Arabidopsis." *PLoS Genetics* 5 (5): e1000492.

Beilstein, Mark A., Kyle B. Renfrew, Xiangyu Song, Eugene V. Shakirov, Michael J. Zanis, and Dorothy E. Shippen. 2015. "Evolution of the Telomere-Associated Protein POT1a in Arabidopsis Thaliana Is Characterized by Positive Selection to Reinforce Protein-Protein Interaction." *Molecular Biology and Evolution* 32 (5): 1329–41.

Birnbaum, Kenneth, Dennis E. Shasha, Jean Y. Wang, Jee W. Jung, Georgina M. Lambert, David W. Galbraith, and Philip N. Benfey. 2003. "A Gene Expression Map of the Arabidopsis Root." *Science* 302 (5652): 1956–60.

Brady, Siobhan M., Lifang Zhang, Molly Megraw, Natalia J. Martinez, Eric Jiang, Charles S. Yi, Weilin Liu, et al. 2011. "A Stele-Enriched Gene Regulatory Network in the Arabidopsis Root." *Molecular Systems Biology* 7 (January): 459.

Chen, Qingchao, Tao Hu, Xiaohua Li, Chun-Peng Song, Jian-Kang Zhu, Liqing Chen, and Yang Zhao. 2022. "Phosphorylation of SWEET Sucrose Transporters Regulates Plant Root:shoot Ratio under Drought." *Nature Plants* 8 (1): 68–77.

Clough, Steven J., and Andrew F. Bent. 1998. "Floral Dip: A Simplified Method forAgrobacterium-Mediated Transformation ofArabidopsis Thaliana." *The Plant Journal: For Cell and Molecular Biology* 16 (6): 735–43.

1226 Crain, Jared, Steve Larson, Kevin Dorn, Traci Hagedorn, Lee DeHaan, and Jesse Poland. 2020.
1227 "Sequenced-Based Paternity Analysis to Improve Breeding and Identify Self-Incompatibility Loci in
1228 Intermediate Wheatgrass (Thinopyrum Intermedium)." *TAG. Theoretical and Applied Genetics.*
1229 *Theoretische Und Angewandte Genetik* 133 (11): 3217–33.
1230 Delude, Camille, Sollapura J. Vishwanath, Owen Rowland, and Frédéric Domergue. 2017. "Root Aliphatic
1231 Suberin Analysis Using Non-Extraction or Solvent-Extraction Methods." *Bio-Protocol* 7 (12): e2331.
1232 Deolu-Ajayi, Ayodeji O., A. Jessica Meyer, Michel A. Haring, Magdalena M. Julkowska, and Christa
1233 Testerink. 2019. "Genetic Loci Associated with Early Salt Stress Responses of Roots." *iScience* 21
1234 (November): 458–73.
1235 Duan, Lina, Daniela Dietrich, Chong Han Ng, Penny Mei Yeen Chan, Rishikesh Bhalerao, Malcolm J.
1236 Bennett, and José R. Dinneny. 2013. "Endodermal ABA Signaling Promotes Lateral Root Quiescence
1237 during Salt Stress in Arabidopsis Seedlings." *The Plant Cell* 25 (1): 324–41.
1238 Fischer, G., Nachtergaele, F. O., Van Velthuizen, H. T., Chiozza, et al. 2021. *Global Agro-Ecological Zones*
1239 *v4 – Model Documentation*. Food & Agriculture Org.
1240 Forsythe, Evan S., Andrew D. L. Nelson, and Mark A. Beilstein. 2020. "Biased Gene Retention in the Face
1241 of Introgression Obscures Species Relationships." *Genome Biology and Evolution* 12 (9): 1646–63.
1242 Foster, Kylie J., and Stanley J. Miklavcic. 2017. "A Comprehensive Biophysical Model of Ion and Water
1243 Transport in Plant Roots. I. Clarifying the Roles of Endodermal Barriers in the Salt Stress Response."
1244 *Frontiers in Plant Science* 8 (July): 1326.
1245 Fu, Yang, Yong Yang, Shaoping Chen, Nina Ning, and Honghong Hu. 2019. "Arabidopsis IAR4 Modulates
1246 Primary Root Growth Under Salt Stress Through ROS-Mediated Modulation of Auxin Distribution."
1247 *Frontiers in Plant Science* 10 (April): 522.
1248 Galvan-Ampudia, Carlos S., Magdalena M. Julkowska, Essam Darwish, Jacinto Gandullo, Ruud A. Korver,
1249 Geraldine Brunoud, Michel A. Haring, Teun Munnik, Teva Vernoux, and Christa Testerink. 2013.
1250 "Halotropism Is a Response of Plant Roots to Avoid a Saline Environment." *Current Biology: CB* 23
1251 (20): 2044–50.
1252 Gehan, Malia A., Noah Fahlgren, Arash Abbasi, Jeffrey C. Berry, Steven T. Callen, Leonardo Chavez,
1253 Andrew N. Doust, et al. 2017. "PlantCV v2: Image Analysis Software for High-Throughput Plant
1254 Phenotyping." *PeerJ* 5 (December): e4088.
1255 Geng, Yu, Rui Wu, Choon Wei Wee, Fei Xie, Xueliang Wei, Penny Mei Yeen Chan, Cliff Tham, Lina Duan,
1256 and José R. Dinneny. 2013. "A Spatio-Temporal Understanding of Growth Regulation during the Salt
1257 Stress Response in Arabidopsis." *The Plant Cell* 25 (6): 2132–54.
1258 Guo, Wei, Limiao Chen, Luis Herrera-Estrella, Dong Cao, and Lam-Son Phan Tran. 2020. "Altering Plant
1259 Architecture to Improve Performance and Resistance." *Trends in Plant Science* 25 (11): 1154–70.
1260 Hassani, Amirhossein, Adisa Azapagic, and Nima Shokri. 2021. "Global Predictions of Primary Soil
1261 Salinization under Changing Climate in the 21st Century." *Nature Communications* 12 (1): 6663.
1262 Höfer, Rene, Isabel Briesen, Martina Beck, Franck Pinot, Lukas Schreiber, and Rochus Franke. 2008. "The
1263 Arabidopsis Cytochrome P450 CYP86A1 Encodes a Fatty Acid Omega-Hydroxylase Involved in
1264 Suberin Monomer Biosynthesis." *Journal of Experimental Botany* 59 (9): 2347–60.
1265 Horton, Matthew W., Angela M. Hancock, Yu S. Huang, Christopher Toomajian, Susanna Atwell, Adam
1266 Auton, N. Wayan Muliyati, et al. 2012. "Genome-Wide Patterns of Genetic Variation in Worldwide
1267 Arabidopsis Thaliana Accessions from the RegMap Panel." *Nature Genetics* 44 (2): 212–16.
1268 Hu, Ying, Qingyu Wu, Stuart A. Sprague, Jungeun Park, Myungmin Oh, C. B. Rajashekar, Hisashi Koiwa, et
1269 al. 2015. "Tomato Expressing Arabidopsis Glutaredoxin Gene AtGRXS17 Confers Tolerance to
1270 Chilling Stress via Modulating Cold Responsive Components." *Horticulture Research* 2 (November):
1271 15051.
1272 Hu, Yunfei, Li Zeng, Xiaodong Lv, Junhua Guo, Xiaoyan Li, Xiaohua Zhang, Dan Wang, et al. 2023.
1273 "NIGT1.4 Maintains Primary Root Elongation in Response to Salt Stress through Induction of ERF1 in

Arabidopsis." *The Plant Journal: For Cell and Molecular Biology* 116 (1): 173–86.
Julkowska, Magdalena M., Huub C. J. Hoefsloot, Selena Mol, Richard Feron, Gert-Jan de Boer, Michel A. Haring, and Christa Testerink. 2014. "Capturing Arabidopsis Root Architecture Dynamics with ROOT-FIT Reveals Diversity in Responses to Salinity." *Plant Physiology* 166 (3): 1387–1402.
Julkowska, Magdalena M., Karlijn Klei, Like Fokkens, Michel A. Haring, M. Eric Schranz, and Christa Testerink. 2016. "Natural Variation in Rosette Size under Salt Stress Conditions Corresponds to Developmental Differences between Arabidopsis Accessions and Allelic Variation in the LRR-KISS Gene." *Journal of Experimental Botany* 67 (8): 2127–38.
Julkowska, Magdalena M., Iko T. Koevoets, Selena Mol, Huub Hoefsloot, Richard Feron, Mark A. Tester, Joost J. B. Keurentjes, et al. 2017. "Genetic Components of Root Architecture Remodeling in Response to Salt Stress." *The Plant Cell* 29 (12): 3198–3213.
Julkowska, Magdalena M., Stephanie Saade, Gaurav Agarwal, Ge Gao, Yveline Pailles, M. Awlia, and M. Tester. 2018. "MVAPP—multivariate Analysis Application for Streamlined Data Analysis and Curation." *Plant Physiology* 23: 44.
Julkowska, Magdalena M., and Christa Testerink. 2015. "Tuning Plant Signaling and Growth to Survive Salt." *Trends in Plant Science* 20 (9): 586–94.
Karcher, Douglas E., Michael D. Richardson, Kenneth Hignight, and Debra Rush. 2008. "Drought Tolerance of Tall Fescue Populations Selected for High Root/shoot Ratios and Summer Survival." *Crop Science* 48 (2): 771–77.
Kassambara, A. n.d. "ggpubr:'ggplot2'Based Publication Ready Plots. R Package Version 0.4. 0." *]. Https://cran-R-Project. Org/web/packages/ggpubr/indes …*.
Kondou, Youichi, Kosuke Noguchi, Shinsuke Kutsuna, Mika Kawashima, Arata Yoneda, Mio Ishibashi, Shu Muto, et al. 2013. "Overexpression of DWARF AND LESION FORMATION 1 (DLE1) Causes Altered Activation of Plant Defense System in Arabidopsis Thaliana." *Plant Biotechnology* 30 (4): 385–92.
Korver, Ruud A., Thea van den Berg, A. Jessica Meyer, Carlos S. Galvan-Ampudia, Kirsten H. W. J. Ten Tusscher, and Christa Testerink. 2020. "Halotropism Requires Phospholipase Dζ1-Mediated Modulation of Cellular Polarity of Auxin Transport Carriers." *Plant, Cell & Environment* 43 (1): 143–58.
Kreszies, Tino, Nandhini Shellakkutti, Alina Osthoff, Peng Yu, Jutta A. Baldauf, Viktoria V. Zeisler-Diehl, Kosala Ranathunge, Frank Hochholdinger, and Lukas Schreiber. 2019. "Osmotic Stress Enhances Suberization of Apoplastic Barriers in Barley Seminal Roots: Analysis of Chemical, Transcriptomic and Physiological Responses." *The New Phytologist* 221 (1): 180–94.
Lampropoulos, Athanasios, Zoran Sutikovic, Christian Wenzl, Ira Maegele, Jan U. Lohmann, and Joachim Forner. 2013. "GreenGate---a Novel, Versatile, and Efficient Cloning System for Plant Transgenesis." *PloS One* 8 (12): e83043.
Laurie, Sophie, Kevin A. Feeney, Frans J. M. Maathuis, Peter J. Heard, Sherralyn J. Brown, and Roger A. Leigh. 2002. "A Role for HKT1 in Sodium Uptake by Wheat Roots." *The Plant Journal: For Cell and Molecular Biology* 32 (2): 139–49.
Lian, Xiaoping, Shilai Zhang, Guangfu Huang, Liyu Huang, Jing Zhang, and Fengyi Hu. 2021. "Confirmation of a Gametophytic Self-Incompatibility in Oryza Longistaminata." *Frontiers in Plant Science* 12 (March): 576340.
Li, Baohai, Takehiro Kamiya, Lothar Kalmbach, Mutsumi Yamagami, Katsushi Yamaguchi, Shuji Shigenobu, Shinichiro Sawa, et al. 2017. "Role of LOTR1 in Nutrient Transport through Organization of Spatial Distribution of Root Endodermal Barriers." *Current Biology: CB* 27 (5): 758–65.
Li, Yonghua, Fred Beisson, Abraham J. K. Koo, Isabel Molina, Mike Pollard, and John Ohlrogge. 2007. "Identification of Acyltransferases Required for Cutin Biosynthesis and Production of Cutin with Suberin-like Monomers." *Proceedings of the National Academy of Sciences of the United States of America* 104 (46): 18339–44.

1322 Lobet, Guillaume, Loïc Pagès, and Xavier Draye. 2011. “A Novel Image-Analysis Toolbox Enabling
1323 Quantitative Analysis of Root System Architecture.” *Plant Physiology* 157 (1): 29–39.
1324 Lu, Kai-Kai, Ru-Feng Song, Jia-Xing Guo, Yu Zhang, Jia-Xin Zuo, Hui-Hui Chen, Cai-Yi Liao, et al. 2023.
1325 “CycC1;1-WRKY75 Complex-Mediated Transcriptional Regulation of SOS1 Controls Salt Stress
1326 Tolerance in Arabidopsis.” *The Plant Cell* 35 (7): 2570–91.
1327 Mäser, Pascal, Brendan Eckelman, Rama Vaidyanathan, Tomoaki Horie, David J. Fairbairn, Masahiro
1328 Kubo, Mutsumi Yamagami, et al. 2002. “Altered Shoot/root Na+ Distribution and Bifurcating Salt
1329 Sensitivity in Arabidopsis by Genetic Disruption of the Na+ Transporter AtHKT1.” *FEBS Letters* 531
1330 (2): 157–61.
1331 Møller, Inge S., Matthew Gilliham, Deepa Jha, Gwenda M. Mayo, Stuart J. Roy, Juliet C. Coates, Jim
1332 Haseloff, and Mark Tester. 2009. “Shoot Na+ Exclusion and Increased Salinity Tolerance Engineered
1333 by Cell Type-Specific Alteration of Na+ Transport in Arabidopsis.” *The Plant Cell* 21 (7): 2163–78.
1334 Munns, Rana, and Mark Tester. 2008. “Mechanisms of Salinity Tolerance.” *Annual Review of Plant*
1335 *Biology*. https://doi.org/10.1146/annurev.arplant.59.032607.092911.
1336 Nelson, Andrew D. L., Evan S. Forsythe, Xiangchao Gan, Miltos Tsiantis, and Mark A. Beilstein. 2014.
1337 “Extending the Model of Arabidopsis Telomere Length and Composition across Brassicaceae.”
1338 *Chromosome Research: An International Journal on the Molecular, Supramolecular and*
1339 *Evolutionary Aspects of Chromosome Biology* 22 (2): 153–66.
1340 Nelson, Andrew D. L., Asher K. Haug-Baltzell, Sean Davey, Brian D. Gregory, and Eric Lyons. 2018. “EPIC-
1341 CoGe: Managing and Analyzing Genomic Data.” *Bioinformatics* 34 (15): 2651–53.
1342 Norris, S. R., S. E. Meyer, and J. Callis. 1993. “The Intron of Arabidopsis Thaliana Polyubiquitin Genes Is
1343 Conserved in Location and Is a Quantitative Determinant of Chimeric Gene Expression.” *Plant*
1344 *Molecular Biology* 21 (5): 895–906.
1345 Ramachandran, Prashanth, Frauke Augstein, Van Nguyen, and Annelie Carlsbecker. 2020. “Coping With
1346 Water Limitation: Hormones That Modify Plant Root Xylem Development.” *Frontiers in Plant*
1347 *Science* 11 (May): 570.
1348 Ranathunge, Kosala, and Lukas Schreiber. 2011. “Water and Solute Permeabilities of Arabidopsis Roots
1349 in Relation to the Amount and Composition of Aliphatic Suberin.” *Journal of Experimental Botany*
1350 62 (6): 1961–74.
1351 Richards, L. A. 1969. *Diagnosis and Improvement of Saline and Alkali Soils*. United States Department of
1352 Agriculture.
1353 Şekerci, Keriman, Nahoko Higashitani, Rengin Ozgur, Baris Uzilday, Atsushi Higashitani, and Ismail
1354 Turkan. 2023. “A Stratagem for Primary Root Elongation under Moderate Salt Stress in the
1355 Halophyte Schrenkiella Parvula.” *Physiologia Plantarum* 175 (3): e13937.
1356 Shukla, Vinay, Jian-Pu Han, Fabienne Cléard, Linnka Lefebvre-Legendre, Kay Gully, Paulina Flis, Alice
1357 Berhin, et al. 2021. “Suberin Plasticity to Developmental and Exogenous Cues Is Regulated by a Set
1358 of MYB Transcription Factors.” *Proceedings of the National Academy of Sciences of the United*
1359 *States of America* 118 (39). https://doi.org/10.1073/pnas.2101730118.
1360 Stamatakis, Alexandros. 2014. “RAxML Version 8: A Tool for Phylogenetic Analysis and Post-Analysis of
1361 Large Phylogenies.” *Bioinformatics* 30 (9): 1312–13.
1362 Team, R. Core, Maintainer R. Core Team, Mass Suggests, and S. Matrix. 2018. “Package Stats.” *The R*
1363 *Stats Package*. https://prs.ism.ac.jp/~nakama/Rjp/stats-manual.pdf.
1364 Uga, Yusaku, Kazuhiko Sugimoto, Satoshi Ogawa, Jagadish Rane, Manabu Ishitani, Naho Hara, Yuka
1365 Kitomi, et al. 2013. “Control of Root System Architecture by DEEPER ROOTING 1 Increases Rice Yield
1366 under Drought Conditions.” *Nature Genetics* 45 (9): 1097–1102.
1367 Ursache, Robertas, Cristovão De Jesus Vieira Teixeira, Valérie Dénervaud Tendon, Kay Gully, Damien De
1368 Bellis, Emanuel Schmid-Siegert, Tonni Grube Andersen, et al. 2021. “GDSL-Domain Proteins Have
1369 Key Roles in Suberin Polymerization and Degradation.” *Nature Plants* 7 (3): 353–64.

1370 Valenzuela, Camilo E., Orlando Acevedo-Acevedo, Giovanna S. Miranda, Pablo Vergara-Barros, Loreto
1371 Holuigue, Carlos R. Figueroa, and Pablo M. Figueroa. 2016. "Salt Stress Response Triggers Activation
1372 of the Jasmonate Signaling Pathway Leading to Inhibition of Cell Elongation in Arabidopsis Primary
1373 Root." *Journal of Experimental Botany* 67 (14): 4209–20.
1374 Wang, Xiaoyang, Yuanming Zhang, Liyuan Wang, Zhaoe Pan, Shoupu He, Qiong Gao, Baojun Chen,
1375 Wenfang Gong, and Xiongming Du. 2020. "Casparian Strip Membrane Domain Proteins in
1376 Gossypium Arboreum: Genome-Wide Identification and Negative Regulation of Lateral Root
1377 Growth." *BMC Genomics* 21 (1): 340.
1378 Wang, Yunbo, Bo Meng, Shangzhi Zhong, Deli Wang, Jianying Ma, and Wei Sun. 2018. "Aboveground
1379 Biomass and Root/shoot Ratio Regulated Drought Susceptibility of Ecosystem Carbon Exchange in a
1380 Meadow Steppe." *Plant and Soil* 432 (1): 259–72.
1381 Weigel, Detlef, and Richard Mott. 2009. "The 1001 Genomes Project for Arabidopsis Thaliana." *Genome*
1382 *Biology* 10 (5): 107.
1383 Wei, T., and V. Simko. 2017. "R Package' Corrplot': Visualization of a Correlation Matrix (Version 0.84)."
1384 *Retrived From, Https://github. Com/taiyun/corrplot*.
1385 West, Gerrit, Dirk Inzé, and Gerrit T. S. Beemster. 2004. "Cell Cycle Modulation in the Response of the
1386 Primary Root of Arabidopsis to Salt Stress." *Plant Physiology* 135 (2): 1050–58.
1387 Wilke, Claus O. 2016. "Cowplot: Streamlined Plot Theme and Plot Annotations for 'ggplot2.'" *CRAN*
1388 *Repos*.
1389 Wu, S. J., L. Ding, and J. K. Zhu. 1996. "SOS1, a Genetic Locus Essential for Salt Tolerance and Potassium
1390 Acquisition." *The Plant Cell* 8 (4): 617–27.
1391 Xu, Wei, Kehui Cui, Aihui Xu, Lixiao Nie, Jianliang Huang, and Shaobing Peng. 2015. "Drought Stress
1392 Condition Increases Root to Shoot Ratio via Alteration of Carbohydrate Partitioning and Enzymatic
1393 Activity in Rice Seedlings." *Acta Physiologiae Plantarum / Polish Academy of Sciences, Committee of*
1394 *Plant Physiology Genetics and Breeding* 37 (2). https://doi.org/10.1007/s11738-014-1760-0.
1395 Yang, Ziheng. 2007. "PAML 4: Phylogenetic Analysis by Maximum Likelihood." *Molecular Biology and*
1396 *Evolution* 24 (8): 1586–91.
1397 Yu, Bo, Wenna Zheng, Lu Xing, Jian-Kang Zhu, Staffan Persson, and Yang Zhao. 2022. "Root Twisting
1398 Drives Halotropism via Stress-Induced Microtubule Reorientation." *Developmental Cell* 57 (20):
1399 2412–25.e6.
1400 Yu, Li 'ang, Hayley Sussman, Olga Khmelnitsky, Maryam Rahmati Ishka, Aparna Srinivasan, Andrew D. L.
1401 Nelson, and Magdalena M. Julkowska. 2023. "Development of a Mobile, High-Throughput, and
1402 Low-Cost Image-Based Plant Growth Phenotyping System." *bioRxiv*.
1403 https://doi.org/10.1101/2023.07.18.549560.
1404 Zarebanadkouki, Mohsen, Pavel Trtik, Faisal Hayat, Andrea Carminati, and Anders Kaestner. 2019. "Root
1405 Water Uptake and Its Pathways across the Root: Quantification at the Cellular Scale." *Scientific*
1406 *Reports* 9 (1): 12979.
1407 Zou, Y., N. Gigli-Bisceglia, E. Zelm, and P. Kokkinopoulou. 2022. "Cell Wall Extensin Arabinosylation Is
1408 Required for Root Directional Response to Salinity." *bioRxiv*.
1409 https://www.biorxiv.org/content/10.1101/2022.06.22.497042.abstract.
1410 Zou, Yutao, Nora Gigli-Bisceglia, Eva van Zelm, Magdalena M. Julkowska, Yuxiao Zeng, Yu Cheng, Iko T.
1411 Koevoets, et al. 2022. "Cell Wall Extensin Arabinosylation Is Required for Root Directional Response
1412 to Salinity." *bioRxiv*. https://doi.org/10.1101/2022.06.22.497042.

1413